Shape Optimization of Vertical-type Probe Needle Integrated with Floating Mount Technology

by

Jiwon Lee

A thesis
presented to the University of Waterloo
in fulfillment of the
thesis requirement for the degree of
Master of Applied Science
in
Mechanical Engineering

Waterloo, Ontario, Canada, 2013

©Jiwon Lee 2013

Author's Declaration

I hereby declare that I am the sole author of this thesis. This is a true copy of the thesis, including any required final revisions, as accepted by my examiners.

I understand that my thesis may be made electronically available to the public.

Abstract

Wafer probing is a testing process to inspect semiconductor wafers before packaging for defects by checking the electrical conductivity via physical contact between the wafers and the probe card. During the contact process, the shape of the probe needle and the mounting configuration onto the probe card have large influences on the stresses and contact force that the probe needles experience. In this paper, static performance of a vertical-type probe needle integrated with floating mount technology is analyzed with a nonlinear finite element analysis. The comparison between fixed mount and floating mount technologies is a part of the analyses. The geometry of a vertical probe needle is optimized to minimize the stress that occurs during the overdrive process, while maintaining adequate force for proper contact with the wafer. Effects of major overall dimensions of probe needle on the maximum stress and contact force is analyzed first, and then curvature of the probe needle body is optimized by employing a constrained minimization function, fmincon, in MATLAB. The maximum stress in the vertical probe pin at 125 μm overdrive is effectively reduced from 1339 MPa to 972 MPa by applying floating mount technology over the fixed mount, and further reduced to 666 MPa by applying the optimization scheme. The final optimized design induced the contact force of 5.217 gf, which is in the range of the required contact force of 5 to 8 gf. Fatigue life increased from 19,219 cycles to 108,129 by applying floating mount over fixed mount, and further increased to 830,596 for the optimized design.

Keywords: wafer probing, probe, probe shape optimization, overdrive

Acknowledgements

I would like to express my sincere gratitude to my supervisor, Professor HJ Kwon, for entrusting me with this research opportunity. He provided me with guidance and support to ensure that I was on the correct path to success, and mentored me with gracious patience, encouragements, and consultations throughout my MASc program. Many thanks also go to Dr. Jeon and project colleagues at Sedicon and SDA Inc: C.S. Han and C.M. Im, for their technical support and providing me with insights from different engineering perspectives.

I would like to thank my project colleague, Dr. Shin, for helping me with my research with technical inputs from his vast industry experience. I would like to thank my lab seniors: Hyunsung Jung, Bonghun Shin, Yougun Han, and Hyunki Bae for not only sharing their technical knowledge but also for sharing their interpersonal knowledge that would help me greatly throughout my life and future career. My thanks also go to Tong Liu for his friendship and creating a supportive working environment.

Finally, I would like to show my deepest thanks to my family for their constant mental support throughout my MASc program.

Table of Contents

Author's Declaration ii
Abstract iii
Acknowledgements iv
List of Figures vii
List of Tables ix
Chapter 1 Introduction 1
1.1 Motivation 1
1.2 Research approach 3
Chapter 2 Literature Review 5
2.1 Probe card 5
2.2 Previous research 6
2.2.1 Cantilever type probe needle 6
2.2.2 Vertical type probe needle 10
2.2.3 Previous fatigue experimentation 14
Chapter 3 Vertical Probe Geometry 16
Chapter 4 Mechanical Property Characterization 18
4.1 Tensile Test 18
4.1.1 Measurement system 18
4.1.2 Specimens 19
4.1.3 True stress and elastic modulus calculation 20
4.2 Atomic force microscopy 21
4.3 Experimental results 21
4.3.1 Probe wire 21
4.3.2 Wafer ball bump 22
Chapter 5 Finite Element Analysis (FEA) Simulation 24
5.1 Simulation scheme 24
5.2 Mesh convergence study 26
5.3 Validation of FEA simulation 27
5.4 Comparison between fixed and floating mount probe assemblies 28
5.5 Contact force (CF) simulation 30
Chapter 6 Probe Geometry Optimization 32

6.1 The effect of overall probe dimensions ... 33
6.2 Design constraints ... 36
6.3 Cobra body curvature optimization ... 37
Chapter 7 Fatigue Analysis ... 42
7.1 Stress versus life (S-N) curve ... 42
7.2 S-N curve approximation ... 43
7.3 Mean Stress Effect ... 43
7.4 Estimation of Fatigue Life ... 44
Chapter 8 Conclusions and Recommendations ... 46
8.1 Conclusion ... 46
8.2 Recommendation ... 47
Bibliography ... 48

List of Figures

Figure 1: SEM view of mini solder ball grid array (Left) [24], and a commercial bump sphere model (unit: μm) (Right) [2]. 1
Figure 2: Close-up view of a probe card with vertical type probe needles (SDA Technology Co., Ltd). 2
Figure 3: Horizontal probe needle used in cantilever type probe cards [25]. 5
Figure 4: Structure of a vertical probe card [3]. 6
Figure 5: Changes in the contact resistance with the number of contacts, using (a) flat tip probe and (b) radius tip probe [15]. 7
Figure 6: Scrub mark lengths under various angles [16]. 8
Figure 7: Tip sliding distance given by model (solid line), scanning electron microscopy measurements (lozenges), and probe mark measurements [7]. 9
Figure 8: Contact resistance of all probe materials at 85 ℃ on an aluminum wafer with a 3-mil overtravel [17] 10
Figure 9: Searching history of von Mises stress and contact force [3]. 11
Figure 10: Influence of the probe diameter D_p on the relation between the vertical contact force F_v and the overdrive δ_{v1} [2]. 12
Figure 11: Buckling mode of a single vertical buckling probe needle (Left) and Probe force versus overdrive (Right) [4]. 12
Figure 12: The geometric structure of the probe (Left), and Diagram of multiple probe array assembly (Right) [26]. 13
Figure 13: (a) The schematic picture of probe's testing mechanism. (b) The fatigue testing set-up of the probe [26]. 15
Figure 14: Geometry model of the vertical cobra probe (left), where O=horizontal offset, T= tip length, I=insert length, H=probe height, and B=cobra body pin length, and deformed vertical probe by the overdrive process (right). 17
Figure 15: Schematics of test set-up for tensile test 19
Figure 16: DIC algorithm tracking the movement of initial markers in the sequential sets of images taken during the tensile test of H3C (Left to right). The red dots and green markers represent the initial and new positions of the markers, respectively 20
Figure 17: True stress-strain curves of H3C obtained from tensile test and DIC 22

Figure 18: (a) AFM image of a wafer bump with 3 points assigned for elastic modulus measurements, and (b) a force-displacement curve from a force spectroscopy 23
Figure 19: FEA simulation of standard probe with floating mount at 125 μm overdrive................... 25
Figure 20: Plot of maximum stress versus number of elements. 26
Figure 21: Plot of contact force versus number of elements... 27
Figure 22: Single probe tester. 27
Figure 23: Plots of contact force from experiment and FEA simulation. 28
Figure 24: Stress distribution across the symmetric section of the probe in (a) a fixed mount, and (b) a floating mount assemblies at 125 μm overdrive. 29
Figure 25: Regions of contact for floating mount assembly at maximum overdrive.......................... 30
Figure 26: (a) Simulation of the wafer bump indentation and (b) the plot of contact force vs. indentation depth.. 31
Figure 27: Overview of the optimization process. 32
Figure 28: Variations of MS (Left) and CF (Right) within the ranges of: (a) horizontal offset, O, (b) cobra body pin length, B, and (c) tip length, T. The third data points in the middle of all plots are the results of the standard design. 34
Figure 29: Performance of (a) MS and (b) CF at 125 μm overdrive, for all designs generated in Table 3. 36
Figure 30: Variations of MS (left) and CF (right) at 125 μm overdrive, with respect to (a) C_1, (b) C_2, and (c) C_3. 38
Figure 31: Illustration of (a) standard design and (b) final optimized design.................................... 41
Figure 32: Schematic of an S-N curve for steels [27] 42

List of Tables

Table 1: Dimensions for the standard probe 17

Table 2: Performance comparison between floating and fixed mount probe assemblies. 30

Table 3: Level assignment to parameters O and T, and the design number for each combination of parameter levels. 35

Table 4: Coefficients of MS (a_i) and CF (b_i) functions estimated by least squares method. 37

Table 5: Comparison of MS and CF values predicted by Eqs. (3) and (4), respectively, and by FEA. 39

Table 6: Optimized coefficients by fmincon, and the predicted MS and CF values by Eqs. (3) and (4), respectively, and by FEA. 40

Table 7: Summary of MS and CF performance at maximum overdrive. 40

Table 8: Summary of factors which reduce the fatigue limit. 43

Table 9: Fatigue life summary 45

Chapter 1
Introduction

1.1 Motivation

As the technology in modern electronics is becoming more advanced, there has been a significant increase in demand for digital technology such as compact, high-density integrated circuits. The semiconductor manufacturers has adapted to the increasing demand by improving the technology in electronic device packaging. For instance, through-hole technology (THT) where electronic components are manually attached to printed circuit boards (PCBs) using lead solders is becoming obsolete for modern electronics, due to their large sizes and low number of input/output (I/O) channels. THT have been largely replaced with surface-mount technology (SMT), where the components are mounted directly onto the PCBs with drastically smaller amount of solders, allowing shorter connection paths and reduced component spacing on PCBs [24]. A widely-used type of SMT is the Ball Grid Array (BGA), which uses a grid of solder ball bumps (also regarded as wafer bump) as the interconnects. The BGA pattern and geometry of each wafer bump is shown in Figure 1.

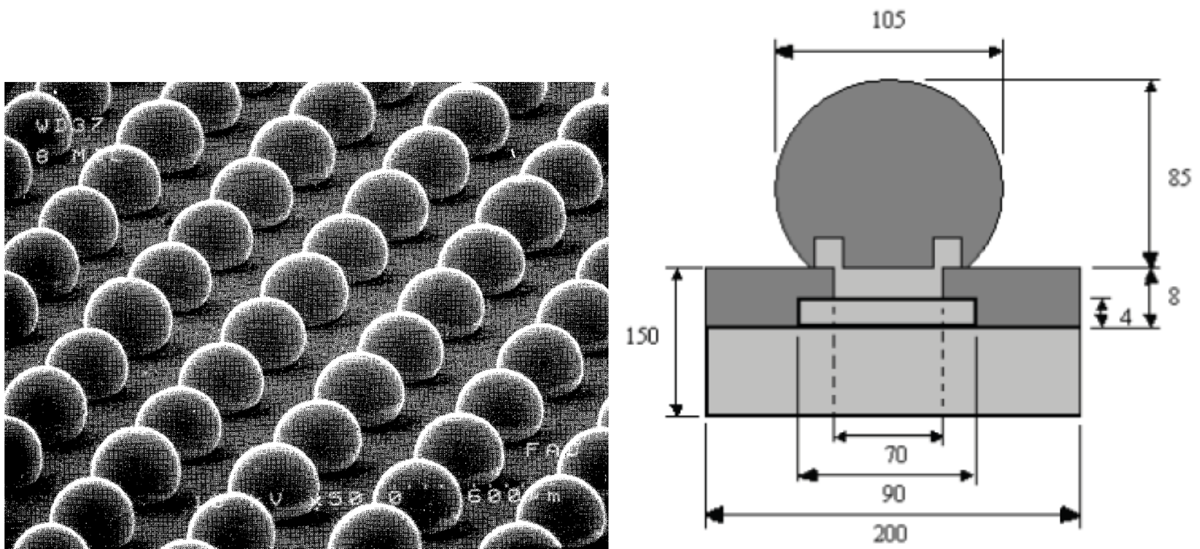

Figure 1: SEM view of mini solder ball grid array (Left) [24], and a commercial bump sphere model (unit: μm) (Right) [2].

Wafer probing is an essential step in semiconductor fabrication which tests a wafer to detect defects before it is sent to die preparation. All individual integrated circuits present on the wafer are tested for functional defects by undergoing wafer probing. The wafer probing is performed by a test apparatus called wafer prober, which holds a probe card in place and manipulates the position of the wafer to ensure precise physical and electrical contact with the probe card, a procedure often regarded as overdrive. Probe card has many probe needles which provide an electrical path between the wafer and the wafer prober, as illustrated in Figure 2. Their free ends are arranged in the same pitch as the array patterns on the BGA.

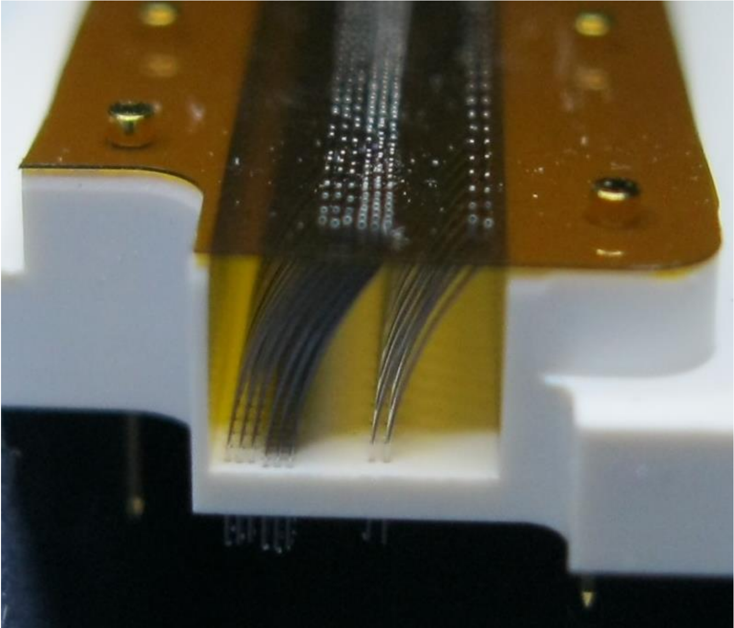

Figure 2: Close-up view of a probe card with vertical type probe needles (SDA Technology Co., Ltd).

The probe needles shown in Figure 2 are oriented vertically; therefore the probe card is regarded as "vertical type". During the overdrive process, the curved design allows the probe needles to buckle during contact, which prevents damage to the wafer bumps by reducing the contact force. To ensure proper testing, the contact force between the needle and the wafer should be large enough to break through the oxide layer, but should not be too large to damage the wafer bump [2]. The probe needles also experience stress due to the deformation caused by buckling, which negatively affects the service life of the overall test equipment. Since the probe needles should sustain over a million touchdowns on the wafer, durability of the probe needles is one of the critical factors in probe card design. It is

clear that the geometry of the probe needles must be designed to minimize stress while providing adequate contact force to ensure proper wafer probing.

In the vertical probe card, a probe needle is not fixed, but is “floating mounted" [14] (Figure 14), in which the upper part is loosely held within a guide hole allowing a small amount of deformation within the hole, and the curvature of the cobra body rests on the top surface of the bottom guide hole of the probe card, preventing the probe needle from falling downwards. This technique does not require the fixing of probe needles and can significantly reduce the stresses experienced by the probe needle during the overdrive process. In addition to probe needle geometry, it is clear that the method in which the probe needles are mounted onto the probe card plays a large role in the maximum stress and contact force.

1.2 Research approach

In this paper, the geometry design of vertical probe needle integrated with floating mount technology was performed by combining nonlinear finite element analysis (FEA) and an optimization method.

A combination of conventional tensile test coupled with optical strain gauge using digital image cross-correlation was employed to determine the material properties of the probe needle material. Force spectroscopy was performed on wafer bump samples to determine its material properties. The obtained material properties were inputted into the FEA models.

A dimensionless 4th order polynomial [3] was employed to represent the cobra body, and the maximum stress in the probe needle and the contact force between the needle and the wafer bump during overdrive operation were analyzed by FEA model. Based on the results from FEA, the maximum stress and the contact force were formulated as functions of the polynomial coefficients by employing least squares method. Using the stress function and the geometry constraint, optimization was conducted to determine the optimal curvature of the probe needle.

For the optimization, the polynomial coefficients were selected as the design variables, with the constraint in the contact force. The optimized geometry can reduce the maximum stress by more than 40% while maintaining the contact force above the minimum required level during overdrive operation.

The fatigue life of the standard and optimized probe designs were analyzed by applying the Juvinall method. The stress-life curve was estimated based on the ultimate tensile strength of the probe material, and the maximum stress obtained from FEA were applied to determine the fatigue lives of the different probe designs.

Chapter 2
Literature Review

2.1 Probe card

One of the most important tasks in semiconductor the semiconductor industry is to develop technologies for quality assurance. The semiconductor wafers are becoming highly integrated and miniaturized, with the number of wafer bumps generated on each chip reaching the thousands. Since any problem on a single bump could cause defects in the final product, the probe card design has evolved to meet the demands to test high number of wafer bumps with high reliability.

Probe cards are classified mainly by the types of probe needles such as vertical type [1-5], cantilever type [6,7], MEMS type [8,9], and etc. Cantilever probe cards contain horizontal needles which are bent downwards at the free end, which comes in contact with the wafer bumps during overdrive (Figure 3). Due to the cantilever probe cards having low pin counts, it is cheap and easy to manufacture and maintain, and make them the most suitable option for specific applications which does not involve large number of wafer bumps. However, the horizontal arrangement of probe needles increase the overall size of the probe card, and makes it difficult to place the needles in complex and dense array patterns. Also, the tip moves horizontally on the wafer bump surface during overdrive, causing damage in forms of scrub marks.

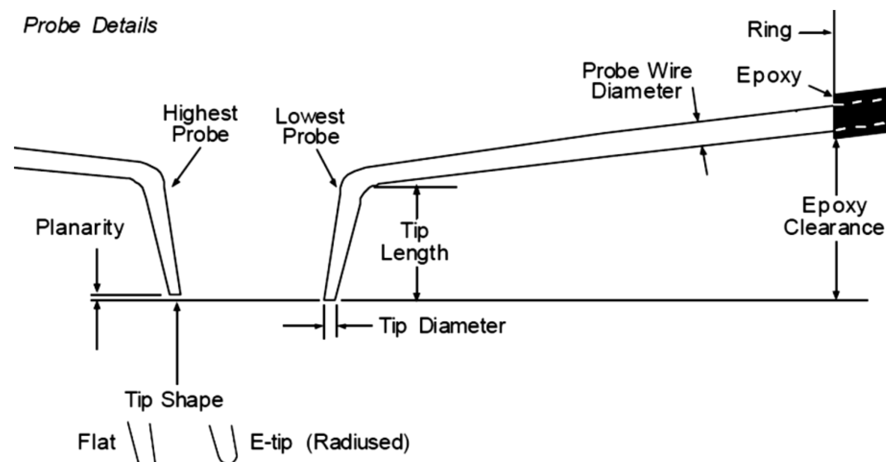

Figure 3: Horizontal probe needle used in cantilever type probe cards [25].

In contrast, probe needles are oriented vertically in a vertical probe card, as illustrated in Figure 4. It is known that vertical type has several advantages over cantilever type such has compactness (it can be applied to area array bumps), uniformity (through the deflection of the probe, contact force on bumps are almost always uniform), maintainability (single probe can be replaced), high-speed wafer level testing and high resolution, and high probe density [3-5, 10-12]. Moreover, the vertical probe card has various design options for different applications, including multilayer ceramic, multilayer organic and wired space transformers [13].

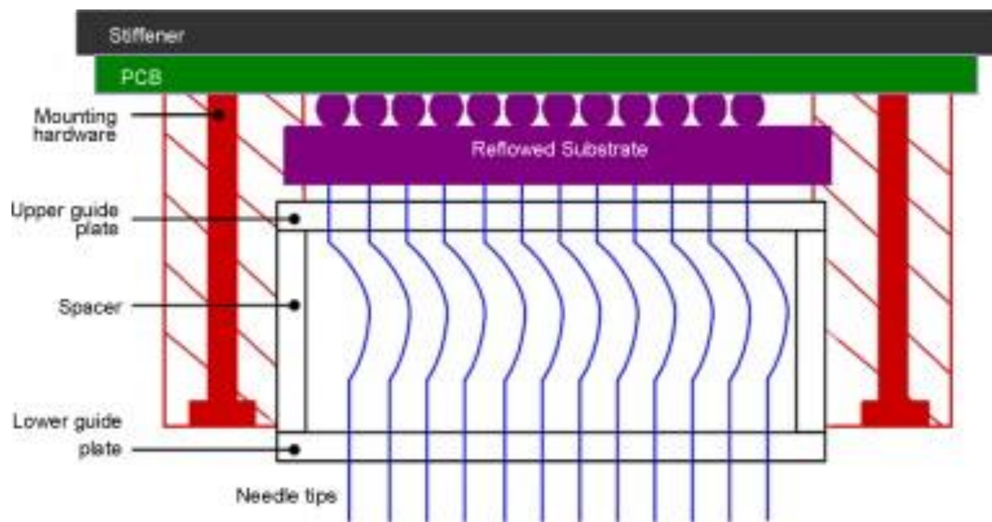

Figure 4: Structure of a vertical probe card [3].

2.2 Previous research

There have been many efforts to analytically or numerically predict the design parameters such as stresses in the probe, the contact force between the needle and wafer, and/or fatigue life. In this section, previous researches which are relevant to this paper are reviewed.

2.2.1 Cantilever type probe needle

A study by Maekawa et al. [15] investigated the relations between tip shape and plastic deformation, and surface roughness and adhesion of aluminum, to improve unstable contact caused by adhesive pick-up of aluminum on the probe tip. In this study, contact resistance was measured during the overdrive between an aluminum alloy wafer and cantilever type probe needles with flat tip shape. It was illustrated that the measured contact resistance became extremely scattered (hundreds of

m Ω to 10 Ω) as the number of contacts were repeated in high numbers (up to 6000), due to the accumulation of aluminum onto the probe tip (Figure 5a). To address this issue, a spherical tip shape was introduced and the optimal radius was experimentally determined to be in the range of 7 to 22 μm (Figure 5b). The heat-treatment conditions for providing optimal needle surface roughness and mechanical properties were also determined (100 MPa, 773 K, 3600 seconds). The methods developed in this study significantly reduced the aluminum accumulation and stabilized the contact resistance measurements throughout high number of contacts.

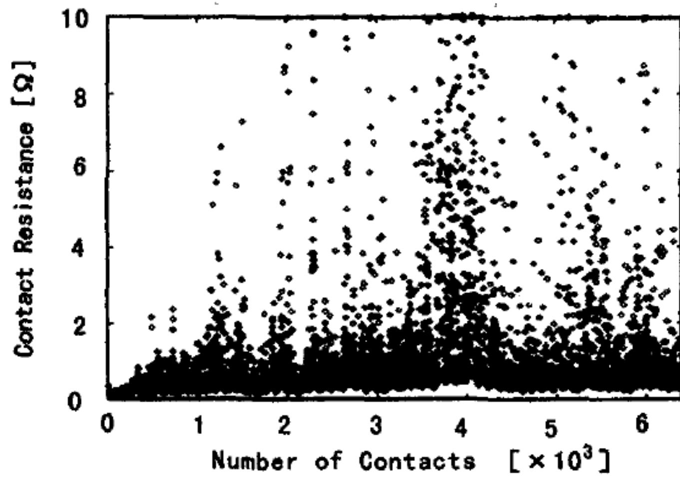

(a)

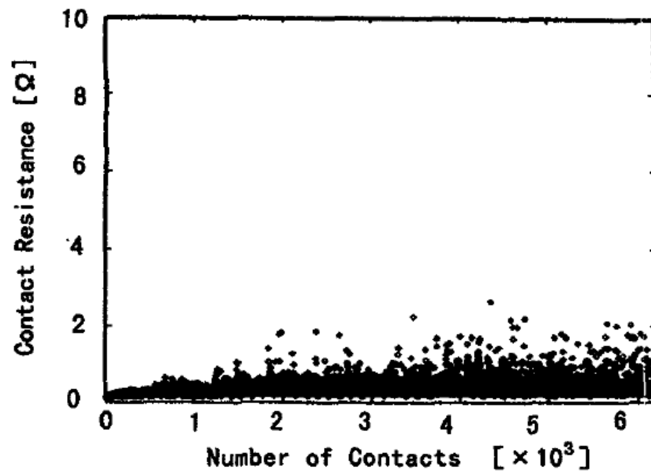

(b)

Figure 5: Changes in the contact resistance with the number of contacts, using (a) flat tip probe and (b) radius tip probe [15].

Chao et al. [16] analyzed the contact phenomena including probe deformation and formation of probing marks on wafer surface, by developing a 3D computational model of the probe and wafer. In this study, mechanical properties of a cantilever type tungsten probe was analyzed via thermal-mechanical tensile test, where a micro-force tester with force range from 0 to 125 N and a displacement resolution of 0.1 microns was attached to thermal chamber providing temperature ranges from 25 to 250 ℃. The elastic modulus of the tungsten probe at various temperature ranges was determined, as well as the contact force and scrub length at various overdrive and bend angles. The mechanical properties obtained from the experiment were inputted as a piece-wise elastoplastic constitutive model into a finite element model in LS-DYNA, and various contact phenomena such as maximum stress on the probe and scrub mark depth and length were modelled. The finite element model was validated by comparing the simulated scrub length to the experiment, as shown in Figure 6.

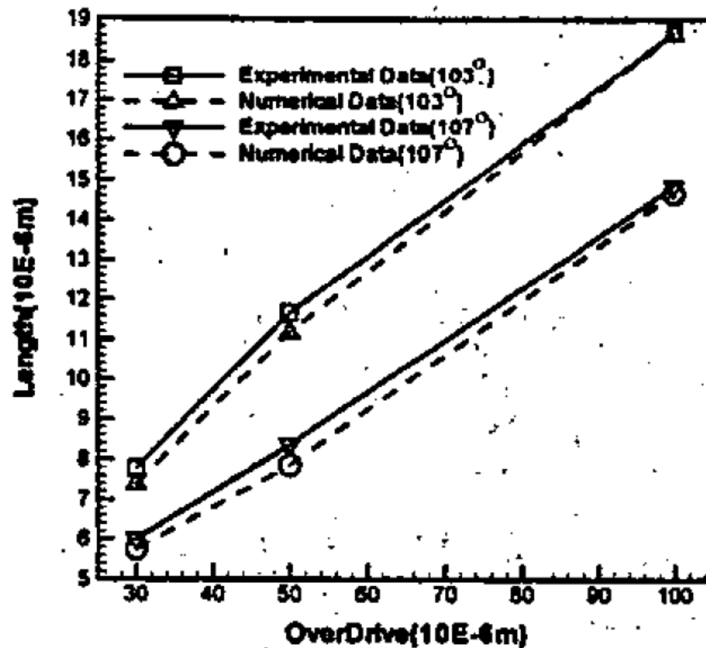

Figure 6: Scrub mark lengths under various angles [16].

Comeau and Nadeau [7] developed an analytical model for calculating the various effects of wafer probing on cantilever type probes. Assuming that the probe is a completely elastic beam, the exact shape of the elastic curve was represented by a nonlinear second-order differential equation, and its exact solution was approximated by applying various boundary conditions related to the overdrive process. Overall, the study provided analytical solution for various key parameters such as total

sliding distance, force, and tip angle variance as a function of beam dimensions and overdrive. The accuracy of the analytical models was verified by comparing the predicted sliding distance from the model with scanning microscopy measurements of actual probe specimen (Figure 7).

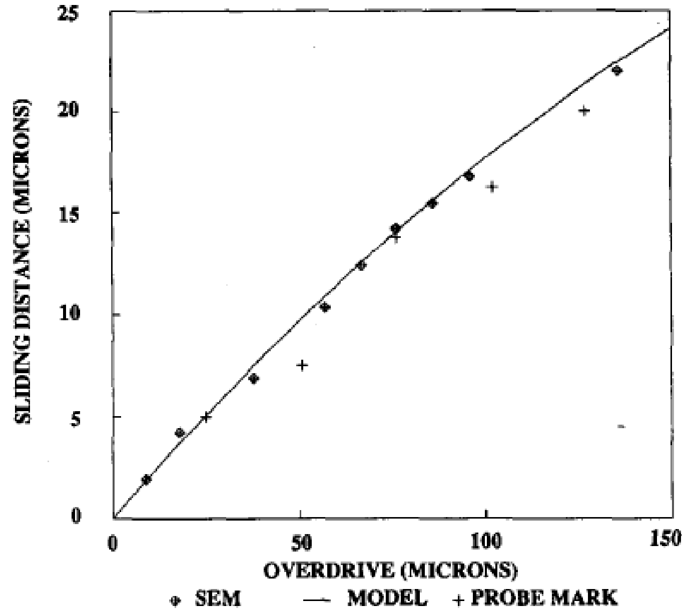

Figure 7: Tip sliding distance given by model (solid line), scanning electron microscopy measurements (lozenges), and probe mark measurements [7].

Broz and Rincon [17] discussed the effects of elevated temperature on the electrical contact between the probe needles of various materials and the wafer during probing process. In this study, several cantilever type probe cards were constructed using probe needles with four different materials: Beryllium-Copper (BeCu), Paliney-7 alloy (Pd-alloy), Tungsten-Rhenium (WRe), and Tungsten (W). The contact resistance was measured during the overdrive between the different probe cards and a substrate with 1-μm thick layer of aluminum at 30 and 85 ℃, for up to 500,000 touchdowns. It was illustrated that the contact resistance of W and WRe probes at 85 ℃ was significantly scattered after only a few thousand touchdowns (Figure 8), but was relatively stable at 30 ℃. The scattering of contact resistance at higher temperature was caused by the formation of oxide layer on the surface of the probe, as well as the additional oxide formation from localized joule heating caused by the measurement current. It was found that the BeCu and Pd-alloy probes did not experience such phenomenon at both 30 and 85 ℃, which suggested that actual high-temperature devices made of

these materials would have decreased continuity failures, reduced cleaning frequency, and less operator intervention.

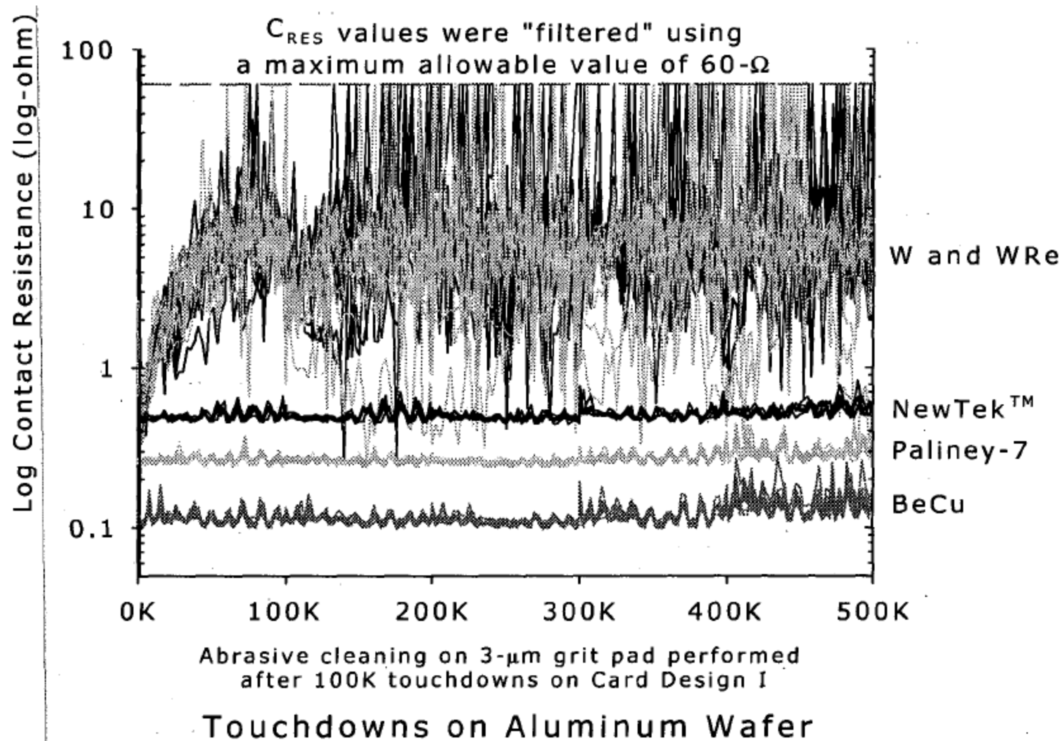

Figure 8: Contact resistance of all probe materials at 85 ℃ on an aluminum wafer with a 3-mil overtravel [17]

2.2.2 Vertical type probe needle

Chiu and Chang [3] derived the optimal geometry design of the vertical cobra body by combining quadratic searching optimization with nonlinear finite element method. In this study, the cobra body was defined as a dimensionless 4th order polynomial (Eq. 1 in Chapter 3), and with the design variable and constraints defined as the geometry and contact force, respectively, the maximum von Mises stress of the probe was minimized through an optimization scheme developed throughout the study. A case study determined the optimal values for the geometry parameters C_1, C_2, and C_3, with the initial values inputted as 0, 1, and 0, respectively, and a contact force of 11 gf. The stress was effectively reduced from 701.1 to 577.4 MPa (17.6% reduction). Figure 1 illustrates the iterations for stress and contact force during the optimization process.

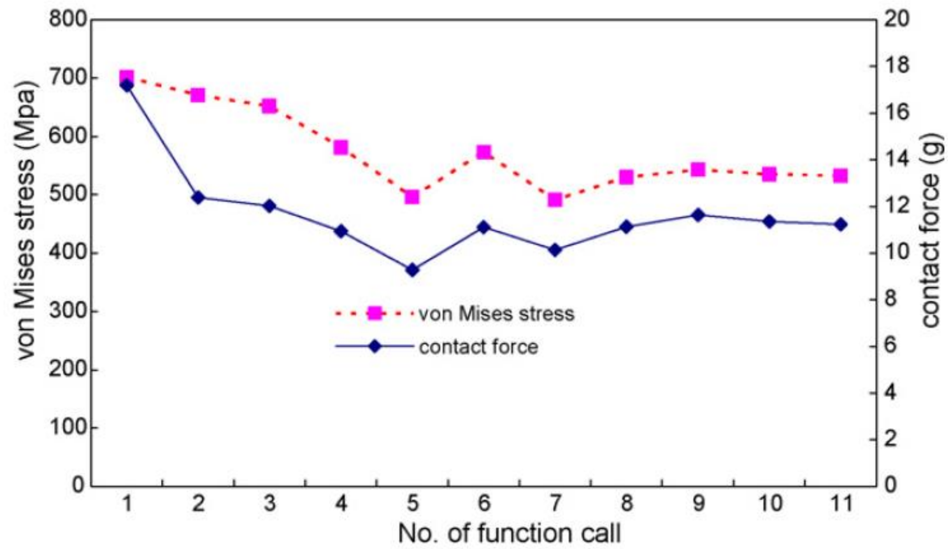

Figure 9: Searching history of von Mises stress and contact force [3].

Chang et al [2] derived relationships among various wafer probing parameters such as contact force, overdrive, probe geometry, material properties, and scrub mark area for a vertical probe card. Elastic-plastic and full plastic analytical models for relating the wafer bump deformation with respect to the contact force and contact area were verified using experimental values and finite element analysis, and it was found that the wafer bump undergoes full plastic deformation during probing. Relationship between contact force and overdrive at various probe needle diameters, as well as the contact force criterion for effective and reliable probing were established using finite element analysis, as indicated in Figure 10.

Hauck and Muller [4] developed an analytical solution for elastic buckling of probe needles by applying the fundamentals of fourth order Euler buckling cases. Analytical solutions were developed for probe force with respect to overdrive for vertical buckling probe needles (Figure 11 (Left)). The analytical model was verified using finite element analysis, where the simulation and empirical showed good correlation, as illustrated in Figure 11 (Right). Also, probe force was measured from an actual probe card, and the measured force was divided by the total number of probe needles then compared with the analytical solutions for a single probe needle. It was observed that the measured force was below the prediction for low overdrive values due to the variance in needle tip planarity.

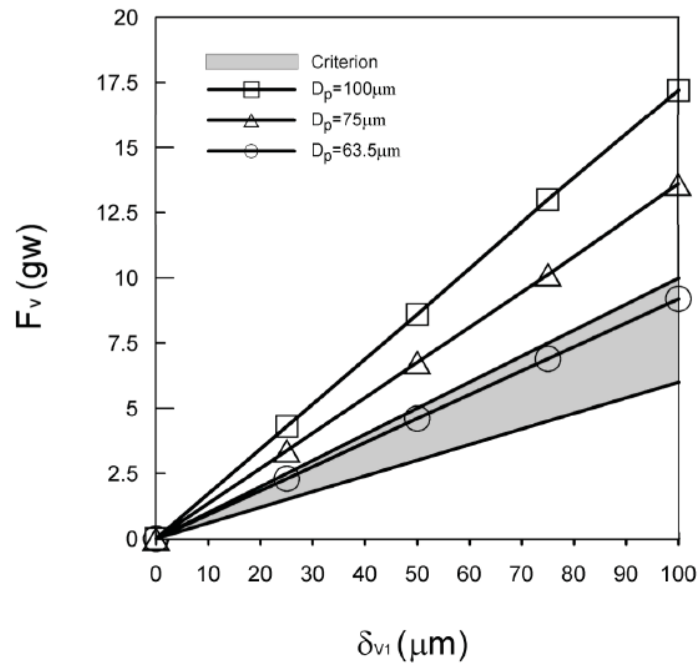

Figure 10: Influence of the probe diameter D_p on the relation between the vertical contact force F_v and the overdrive δ_{v1} [2].

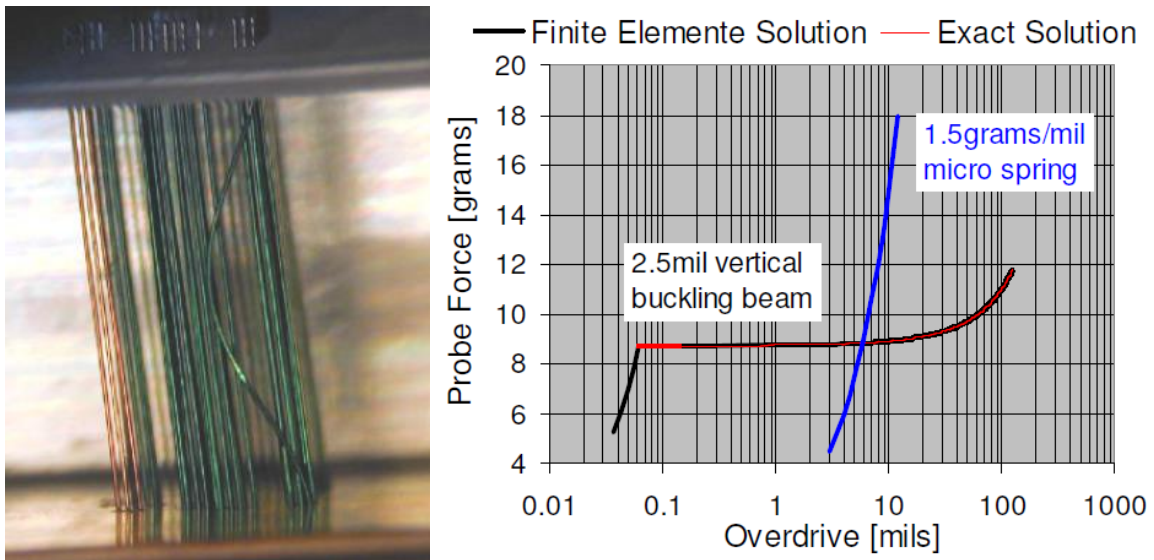

Figure 11: Buckling mode of a single vertical buckling probe needle (Left) and Probe force versus overdrive (Right) [4].

Huang et al [26] analyzed the loading force distributed on the vertical probe tip by employing COSMOS finite element simulation software, and developed methods for manufacturing probes with optimal hardness, elastic modulus, and fatigue strength. In this study, the vertical probe geometry was defined with two curvatures with radius R1 and R2 as shown in Figure 12 (Left). Various combinations of R1 and R2 were tested via COSMOS, and the optimal design that minimizes stress and scrub distance was determined. Methods for fabricating probe cards at low cost and high precision was discussed, such as multiple probe array assembly shown in Figure 12 (Right). A MEMS probe card was developed which combines micro-electroplating and chemical mechanical polishing processes to manufacture high-performance vertical probe needles.

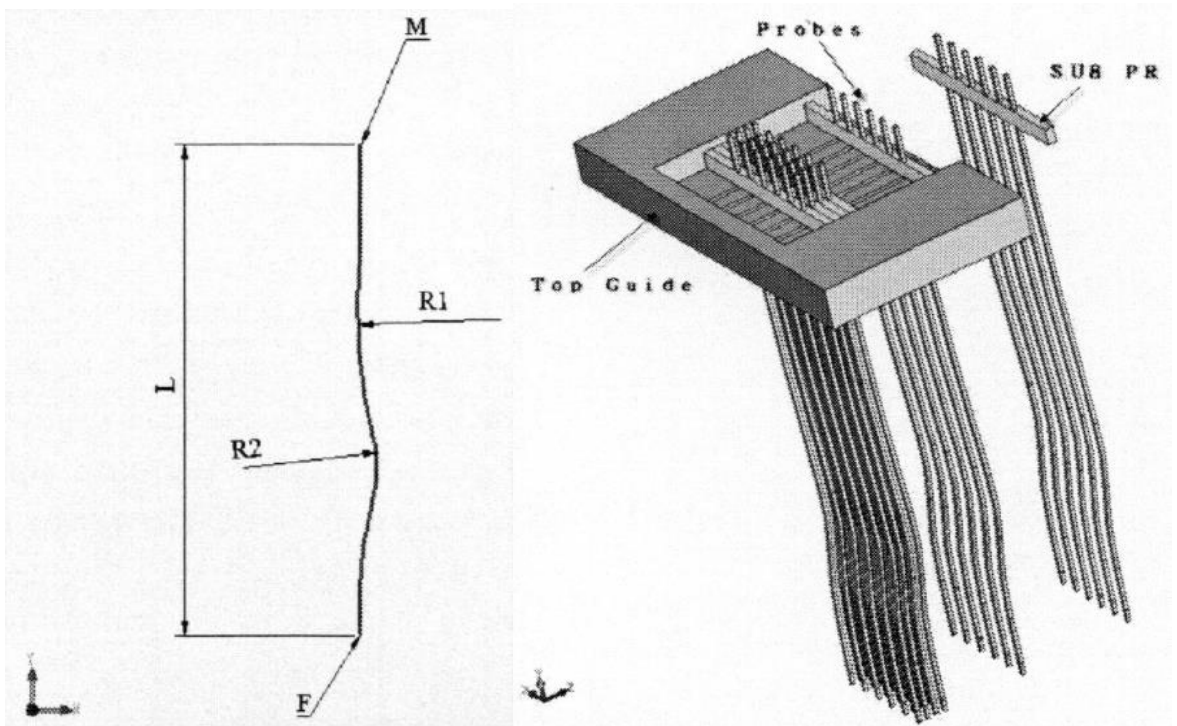

Figure 12: The geometric structure of the probe (Left), and Diagram of multiple probe array assembly (Right) [26].

2.2.3 Previous fatigue experimentation

Very little study has been performed on the fatigue failure of the probe needle, mainly due to the difficulty in the experiment. One of them was performed by Huang et al [26], who performed fatigue test on buckling vertical probe pins (Figure 12 (Left)) which underwent electroplating and chemical mechanical polishing. The reciprocating motion was induced to the probe pin by a voice coil motor which was connected to microcontroller for varying vibration speed. Voice coil motor was used due to its fast response speed. Laser measuring system was used to record the displacement of the motor, which was equivalent to the deformation of the probe. A force sensor recorded the contact force of the probe caused by the overdrive. The schematic of the fatigue testing system and the actual experiment set-up is provided in Figure 13(a) and (b), respectively.

The Young's modulus and hardness values were 180 GPa and HV 550, respectively. 45 μm of overdrive at a contact force of 4g was applied repeatedly the probe needle, and it was determined that the fatigue strength was higher than 1 million cycles.

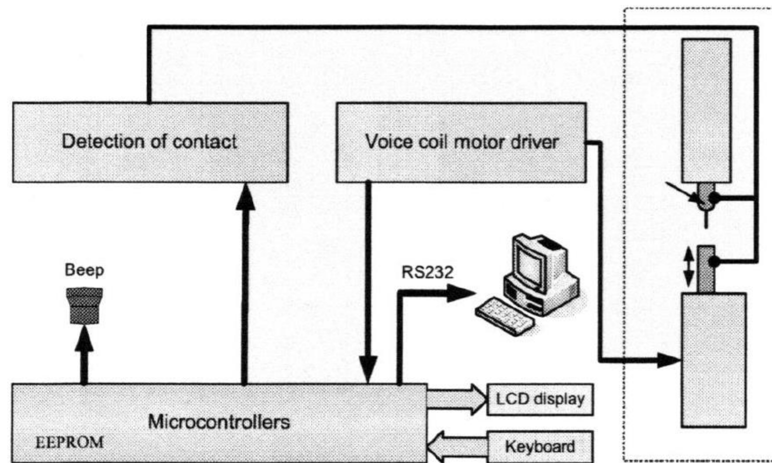

(a)

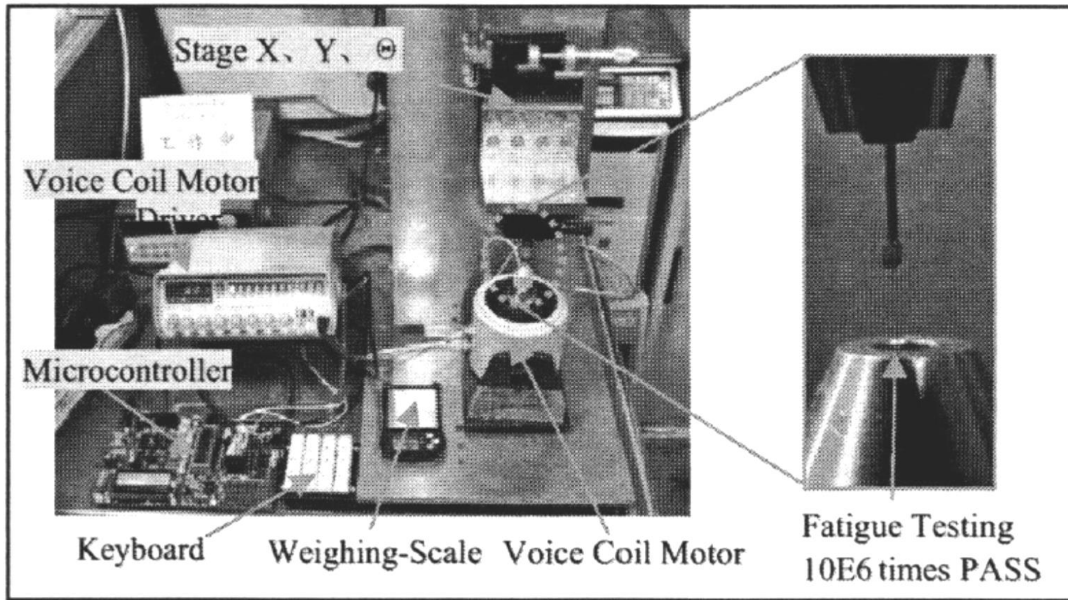

(b)

Figure 13: (a) The schematic picture of probe's testing mechanism. (b) The fatigue testing set-up of the probe [26].

Chapter 3
Vertical Probe Geometry

This study focuses on the analysis and optimization of a vertical type probe needle called "cobra pin", provided by Sedicon Co., Ltd. This probe needle is the basis of the study - modifications will be made to this design in order to optimize the parameters such as contact force and maximum stress.

Vertical probe is mainly divided into three parts (Figure 14 Left): needle tip for contacting with a wafer on a probed die; insert part for locating and insertion of the probe onto a probe card; and cobra body being disposed between the needle tip and the insert part. The cobra body is stamped from a pre-curve wire rod with a flat rectangle section. The axial direction of needle tip and insert part has an offset, and both are aligned by cylindrical guide holes which are cut into the probe card. In probing operation, when the needle tip contacts the wafer, the cobra body is deformed by bending and buckling actions (Figure 14 (Right), which provides necessary contact force for probing. Vertical probe usually alters the horizontal offset (O in Figure 14 (Left)) or the cobra body pin length (B in Figure 14 left) to derive the expected contact force. The dimensions for the standard probe are listed in Table 1.

Furthermore, it was proposed by Chiu et al. [3] that the geometry of the curvature for a vertical probe can be expressed by a dimensionless 4th order polynomial:

$$\frac{y(z)}{O} = C_1\left(\frac{z}{B}\right) + C_2\left(\frac{z}{B}\right)^2 + C_3\left(\frac{z}{B}\right)^3 + (1 - C_1 - C_2 - C_3)\left(\frac{z}{B}\right)^4 \qquad (1)$$

where B and O are cobra body pin length and horizontal offset, respectively and C_1, C_2, and C_3 are dimensionless polynomial coefficients ranging from -2.0 to 2.0. It was stated that parameters C_1, C_2, and C_3 affect the shape of upper, mid, and lower sections of the probe, respectively.

Since the cobra body is bent and buckled during overdrive, high stress is developed locally by stress concentration, which can exceed the yield stress of the material. Also the maximum stress has a direct influence on the fatigue life of the probe. Therefore, there is a strong need to optimize the overall shape and curvature of the vertical probe, so that the stress caused by overdrive process is suppressed below the yield and fatigue limits while suitable level of contact force is developed, which is the goal of the design optimization in this paper.

Table 1: Dimensions for the standard probe

Parameter	O	B	W	L	D	T	I
Dimensions (mm)	0.994	2.797	0.085	0.038	0.0635	1.100	0.600

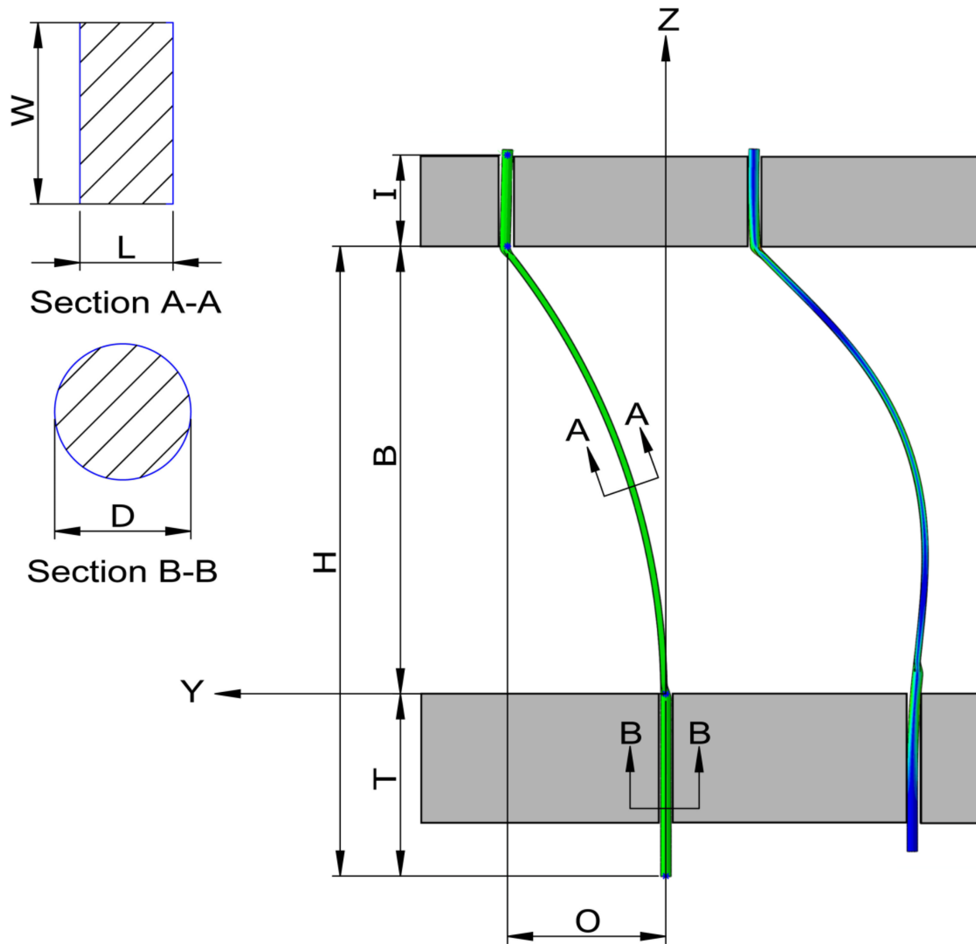

Figure 14: Geometry model of the vertical cobra probe (left), where O=horizontal offset, T= tip length, I=insert length, H=probe height, and B=cobra body pin length, and deformed vertical probe by the overdrive process (right).

Chapter 4
Mechanical Property Characterization

Prior to performing finite element analysis, the material properties of the probe were analyzed. Probe material specimen was available in the form of a very thin wire, and preliminary tensile tests showed that the ductility of the material was low. The amount of deformation from gripping the sample will be very large compared to the sample's small diameter, which would mean that the results from a standard tensile test would be highly susceptible to the effects of stress concentration at the gripped area. The standard tensile test procedure was accompanied by optical strain gauge technique using digital image cross-correlation to suppress such effects. Wafer bump sample was available in a BGA sample, and since tensile test was not feasible, atomic force microscopy was used to analyze its material properties.

4.1 Tensile Test

4.1.1 Measurement system

To measure the mechanical properties of the probe material, tensile tests were performed on Paliney® H3C (High-Hardness/High Conductivity) wire specimens using a TA micro testing machine (TA.xt Plus, Stable Micro Systems) with a 5 kgf load cell. Force, displacement, and time data were collected via the controlling computer. The images of the mid-section of the H3C wire were captured during the tensile test at 3 frames per second, using a high resolution CCD camera (1028x1008 pixels, STC-CL202A, Sentech) via 20x objective lens. Tensile test data and the captured images were synchronized using a custom-developed LabVIEW (National Instrument) code. To prevent localized deformation and stress concentrations at the gripping sections, the ends of the wire specimens were wound around the threads of two steel bolts, and the two ends of the wire specimen were held by the grippers.

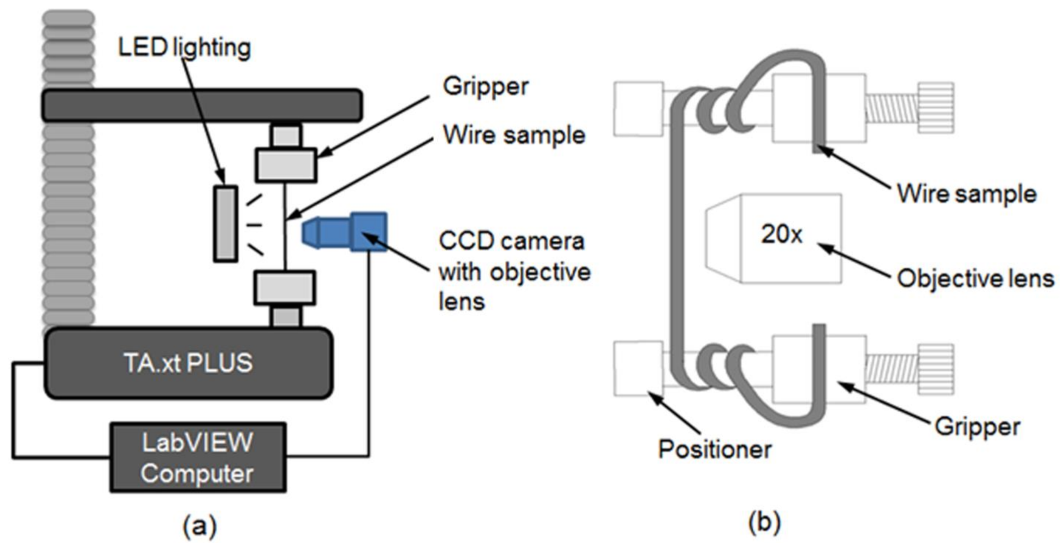

Figure 15: Schematics of test set-up for tensile test

4.1.2 Specimens

Tensile tests were performed on a H3C wire from which the probe pins are stamped into their functional forms. Specimens were prepared by cutting H3C wire (Deringer-Ney, USA) to have 90 mm length. Diameters of 20 different specimens were measured using a micrometer (Mitutoyo Series 293, 1 μm resolution). 5 measurements were taken per specimen at varying locations and angles along the specimen's length. It was observed that the specimen has almost perfect circular cross-section with a consistent diameter of 63.5 μm (±1 μm maximum variation). Due to the sample's small diameter, it was predicted that the local stress concentration at the gripping area would have a significant effect on the results, despite the efforts to suppress such stresses (Figure 15b). To avoid this, digital image cross-correlation (DIC) technique was employed for strain measurement. The surface of the specimen was pre-treated with a thin coating of black laser toner for DIC pattern tracking.

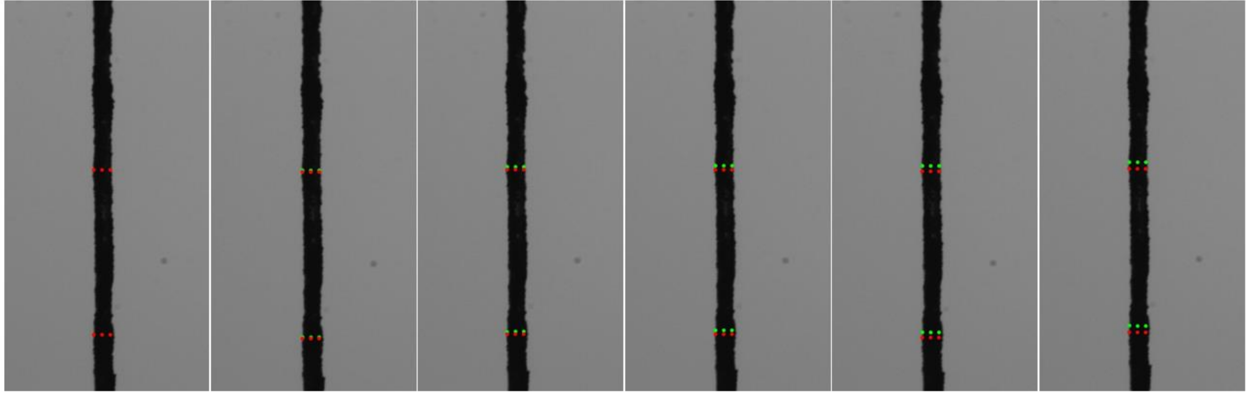

Figure 16: DIC algorithm tracking the movement of initial markers in the sequential sets of images taken during the tensile test of H3C (Left to right). The red dots and green markers represent the initial and new positions of the markers, respectively.

4.1.3 True stress and elastic modulus calculation

By applying the custom-developed DIC to the images of specimen captured during the test, displacements in the mid-section could be determined. From the force-displacement data, engineering stress (σ_E)-engineering strain (ε_E), and true stress (σ_T)-true strain (ε_T) plots were generated using the following formula:

$$\varepsilon_E = \frac{\Delta L}{L_0}, \qquad \varepsilon_T = \ln(\varepsilon_E + 1)$$
$$\sigma_E = \frac{F}{A_0}, \qquad \sigma_\mathrm{T} = \sigma_E \frac{1+\varepsilon_E}{1+(1-2\nu)\varepsilon_E} \tag{2}$$

where L_0 is the initial length, and ΔL elongation. Poisson's ratio ν of 0.38 provided by material producer was used for the calculation. The same types of plots were also generated by the tensile test, i.e., using the displacement between the grippers as ΔL in Eq. (2). This plot was used only for reference to be compared with that from DIC.

4.2 Atomic force microscopy

To measure the mechanical properties of the wafer bump, force spectroscopy was performed on 63%Sn-37%Pb wafer bump specimens using atomic force microscopy (AFM) (XE 100, Parks System). The wafer bump specimens were fixed securely onto the specimen plate. Force spectroscopy images were acquired in contact mode in air medium, using a contact cantilever with thickness of 2 μm, mean with of 50 μm, length of 450 μm, force constant of 0.2 N/m, resonance frequency of 13 kHz, and a pyramidal tip shape (PointProbe®Plus Contact Mode, Nanosensors). Force-distance curves were collected from 8 different wafer bumps. For each wafer bump, 3 measurements were made at varying locations in a 6 μm x 6 μm area, with force limit between 1.24 nN to 1.5 nN, deformation depth between 300 nm to 500 nm, and frequency of 0.5 kHz.

4.3 Experimental results

4.3.1 Probe wire

The true stress-strain curves obtained from the tensile tests and DIC method for H3C wire are presented in Figure 17. Both curves showed linear stress-strain behavior in the region up to 0.01 strain, with the curve from DIC positioning higher than that from the conventional tensile test. They became slightly nonlinear until it was failed in a brittle manner.

Elastic modulus was estimated to be 109 GPa and 121 GPa by the tensile test and DIC, respectively, in the linear elastic region between 0.0005 and 0.002 strain. Note that despite the efforts to suppress the local deformation and slip by using custom-developed gripper, strain seemed to be overestimated in the conventional tensile test, as indicated by the lower stress at the same strain than that from DIC. Since DIC could eliminate these errors in strain measurement, the stress-strain curve from DIC was deemed to be reliable. Therefore, elastic modulus of 121 GPa estimated by DIC was employed in all FEA simulations.

By using 0.2% offset line from the stress-strain curve in the linear region, yield stress was estimated to be approximately 1500 MPa which was consistent with manufacturer's data of 1482 MPa. Ultimate strength was estimated to be approximately 1820 MPa.

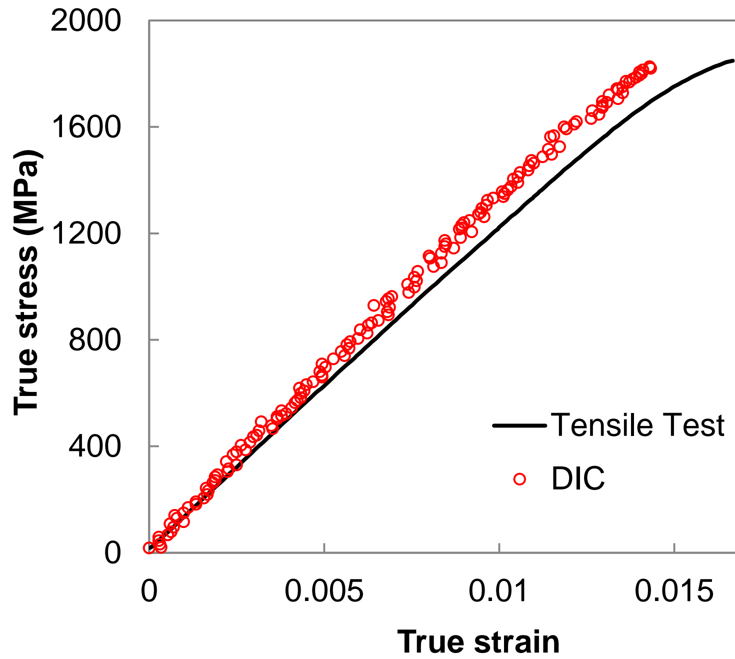

Figure 17: True stress-strain curves of H3C obtained from tensile test and DIC

4.3.2 Wafer ball bump

Force spectroscopy images were taken from 8 wafer ball bumps (Figure 18(a)), and elastic moduli at 3 different points for each image were estimated from force-displacement curves (Figure 18(b)) using Hertzian model. From the total of 24 measurements, average elastic modulus was estimated to be 28.46 GPa with the standard deviation of 5.18 GPa. Since the measurements were very local, the measured values showed some scattering; however, the errors were in acceptable range and they were consistent among the bumps. This measured value is lower than the ASTM Standard (B 32 Grade) of 32 GPa, because the wafer ball bumps were tested up to depth of approximately 30 nm by the AFM, where the oxide layer accumulated at the surface would have a predominant effect on the material properties. Since the depth of indentation from wafer probing occurs at surface level, and is insignificant compared to the entire diameter of the wafer bump, it is reasonable to employ the elastic modulus measured by the AFM to the simulation model. The average of all measurements (28.46 GPa) was employed as the elastic modulus in the linear elastic-linear work-hardening material model of 63%Pb-37%Sn solder for FEA simulations. Poisson's ratio of 0.38 and the work-hardening modulus

of 28.125 MPa, provided by ASTM Standards (B 32 Grade), were also adopted for the simulation model.

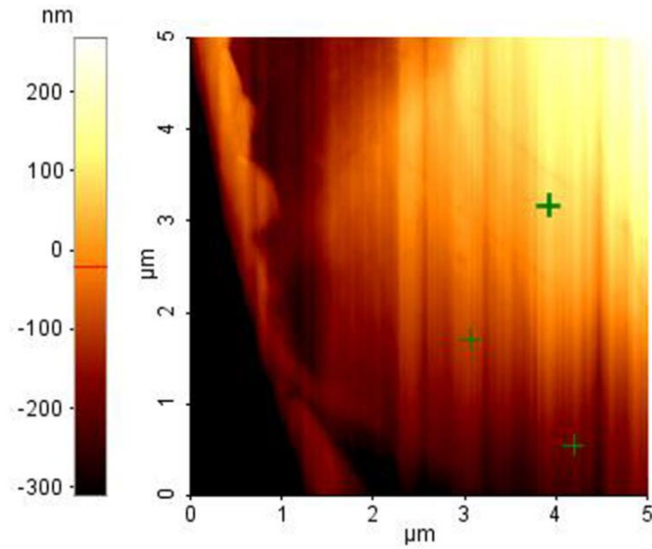

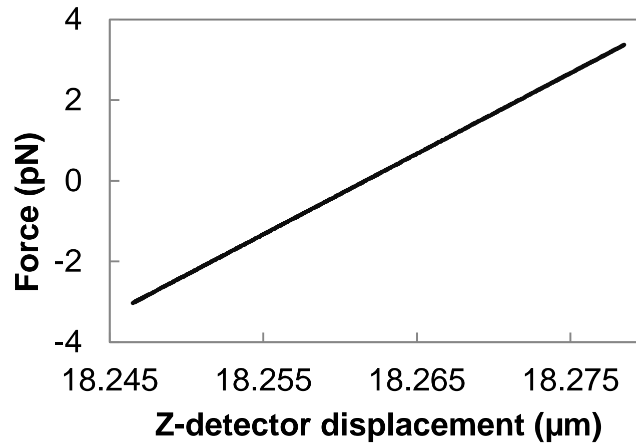

(b)

Figure 18: (a) AFM image of a wafer bump with 3 points assigned for elastic modulus measurements, and (b) a force-displacement curve from a force spectroscopy

Chapter 5
Finite Element Analysis (FEA) Simulation

Due to the probe needle's small size and complexity in mounting, measuring the stresses during the overdrive process through experimentation was not feasible. In addition, numerous different probe designs had to be tested for the optimization scheme in the later chapters. Therefore, finite element analysis was employed to predict the stresses and the contact forces in the probe designs. Detailed models of the probe needle was developed using 3D computer-aided design software (SolidWorks), and the models were imported to a commercial finite element code for further analysis. Mesh convergence study was conducted to minimize computational resources, and the validity of the finite element model was verified by comparing its contact force results to an actual probe needle. The relationship between the contact force and the amount of wafer bump deformation was also analyzed in a separate model.

5.1 Simulation scheme

Finite element analysis (FEA) was performed using a commercial FEA code (Abaqus/CAE 6.10) on the overdrive process of probe assembly models employing the boundary conditions which mimicked the actual wafer probing process. The floating mount assembly constrained only the movement in y-direction and allowed the deformation within the cylindrical guide (Figure 19). Detailed boundary conditions of floating mount assembly were defined as follows:

- Insert part was housed concentrically within a rigid guide cylinder with 80 μm diameter and 550 μm height. Surface-to-surface contact condition with coefficient of friction of 0.12 (Steel and ceramic with lubrication) [18] was defined between the outer surface of the insert part and the inner surface of the guide cylinder.
- Needle tip was housed concentrically within a rigid guide cylinder with 80 μm diameter and 700 μm height, with identical surface-to-surface contact condition as the insert.
- Movement/deformation of the insert part and the needle tip in the horizontal directions were suppressed by the guide cylinders once contact was made.
- Bottom surface of the needle tip was moved upwards by 125 μm, simulating the overdrive process, while top surface of the insert part was fixed in the vertical direction.

Fixed mount probe assembly was also modeled by constraining all movements, and hence, restricting any deformation, in the insert part (I in Figure 14 (Left)).

All models were meshed with an average of 18,000 3D hexahedral elements and 24,000 nodes (Figure 19). Maximum stress (MS) was defined as the highest Mises stress in the model at the maximum overdrive, and the contact force (CF) was measured at the bottom surface of the needle tip at that moment.

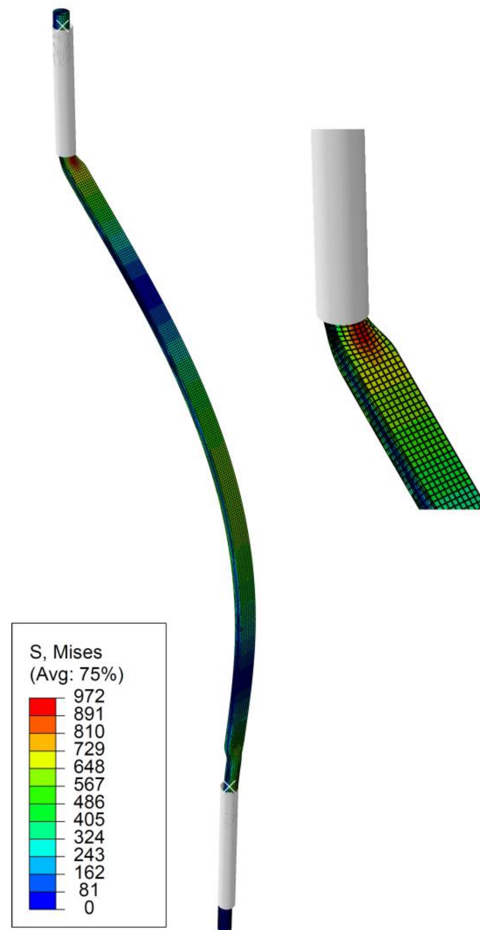

Figure 19: FEA simulation of standard probe with floating mount at 125 μm overdrive.

5.2 Mesh convergence study

Mesh convergence study was performed in order to conserve computation time while ensuring that the FEA models provided reliable solutions. This was a crucial step since the probe geometry optimization in Section 5 required performing multiple simulations (up to 15), and the optimization results were heavily dependent on the FEA models. The mesh was refined until convergence was observed from solutions for both MS and CF. Number of elements ranging from approximately 1000 to 35000 were tested. Aspect ratios of the mesh at all refinement stages were conserved to be approximately 1 to prevent interpolation errors. The study was performed on the floating mount assembly with standard probe design, with boundary conditions specified in Section 5.1. The MS and CF results with varying number of elements were plotted in Figure 20 and Figure 21, respectively.

Convergence was observed for both MS and CF results at 17796 elements which are indicated by the red data point in Figure 20 and Figure 21. The difference in MS and CF results from FEA models with 17796 to 34296 elements was only 3.86% and 0.37%, respectively, while computation time increased by a factor of 2.7 (from 30 to 80 minutes). Therefore, it was concluded that using approximately 18000 elements for all models would provide acceptable solutions for MS and CF while minimizing computation time.

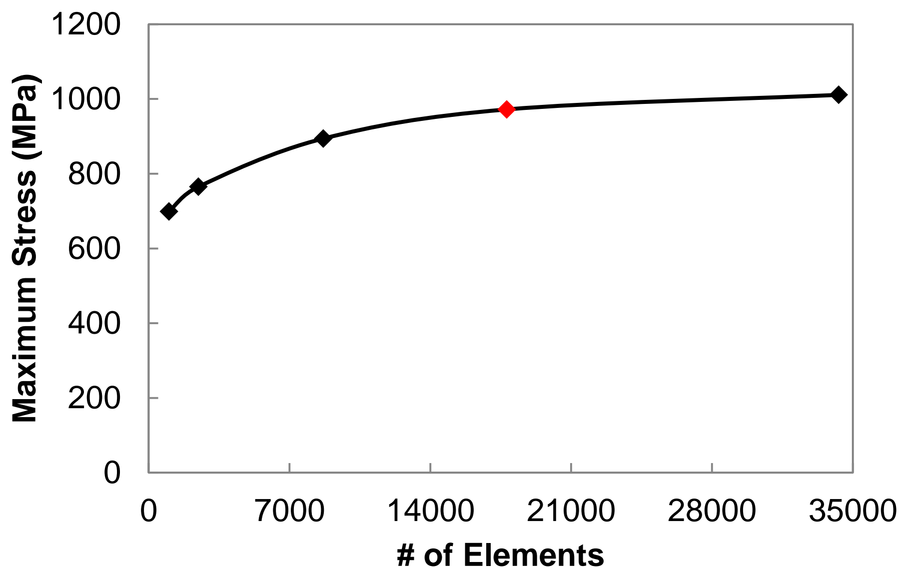

Figure 20: Plot of maximum stress versus number of elements.

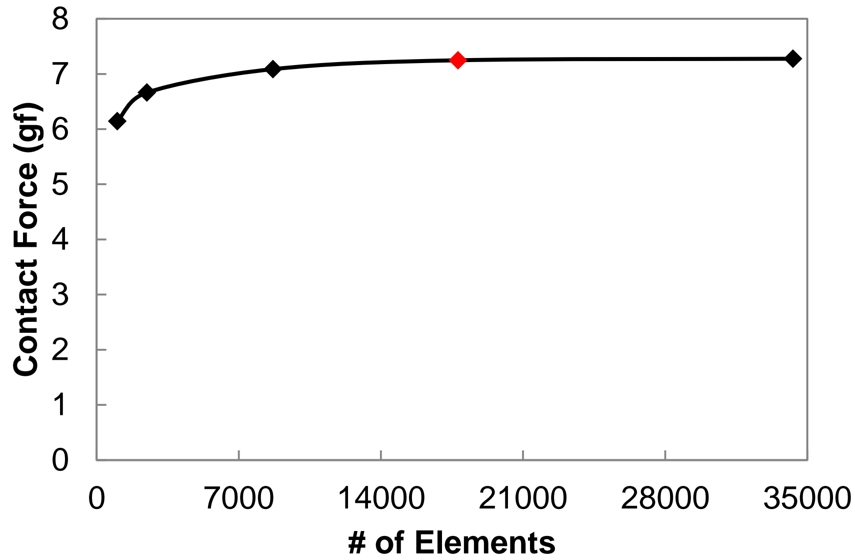

Figure 21: Plot of contact force versus number of elements.

5.3 Validation of FEA simulation

The validity of the FEA was verified by performing the experiment mimicking the overdrive process of the probe needle and comparing the results with those from the simulations on the same process. In the experiment, overdrive was applied to an actual standard probe specimen using a TA micro testing machine with 1 kgf load cell. Force, displacement, and time data were collected via the controlling computer. A testing rig which holds a single probe specimen within a set of guides with identical geometry and position as the floating mount FEA simulations was specially designed for this experiment (Figure 22). The probe specimen is pointed by an arrow in Figure 22.

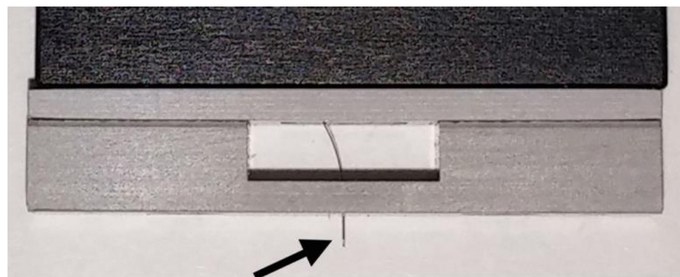

Figure 22: Single probe tester.

The CFs measured from the experiment and predicted by FEA were plotted with respect to the overdrive in Figure 23. Both results exhibited similar trends, with only a small amount of deviation occurring from 75 μm to 125 μm overdrive. The maximum deviation was approximately 7% at peak overdrive where CF was the highest, which could have resulted from the clearance error of the guide holes during machining of the single probe tester. The good agreement between the experiment and simulation suggested that the FEA simulation is reliable enough to be used for the optimization in the following sections.

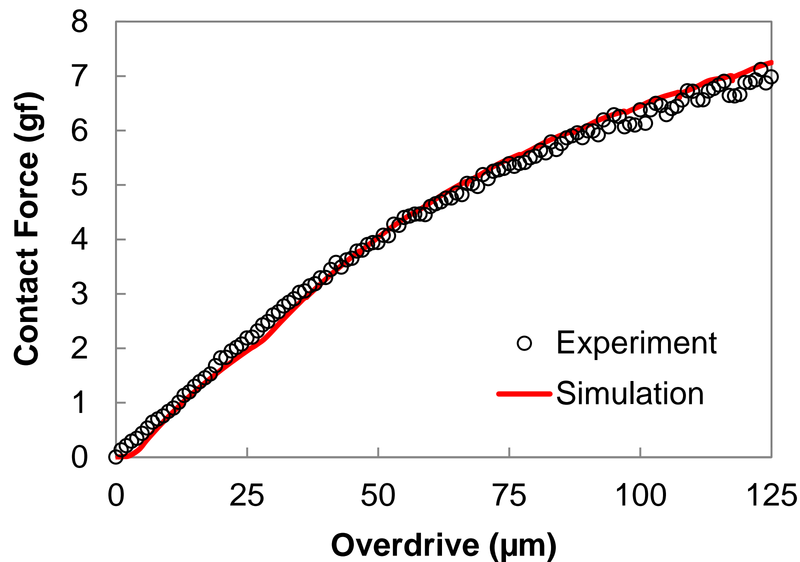

Figure 23: Plots of contact force from experiment and FEA simulation.

5.4 Comparison between fixed and floating mount probe assemblies

As a preliminary step for design optimization, the effect of mounting method was investigated by performing FEA simulations on fixed and floating mount probe assemblies for standard probes.

In the simulations for both types of mount assemblies, MS occurred at the bent region near where the transition occurred between insert part and cobra body. Figure 24 shows the stress distribution across the symmetric section of the probe needle in each mounting type. For fixed mount assembly, since no deformation was allowed in the insert part, stress was highly concentrated at the transition region (Figure 24(a)). On the other hand, in floating mount assembly, stress was distributed throughout insert part due to the small deformation allowed inside the guide cylinder, and hence, the

maximum stress at the transition region was significantly reduced, as illustrated in Figure 24(b). It was also confirmed that MS in both assemblies were lower than yield stress; thus yielding did not occur and linear elastic analysis was acceptable.

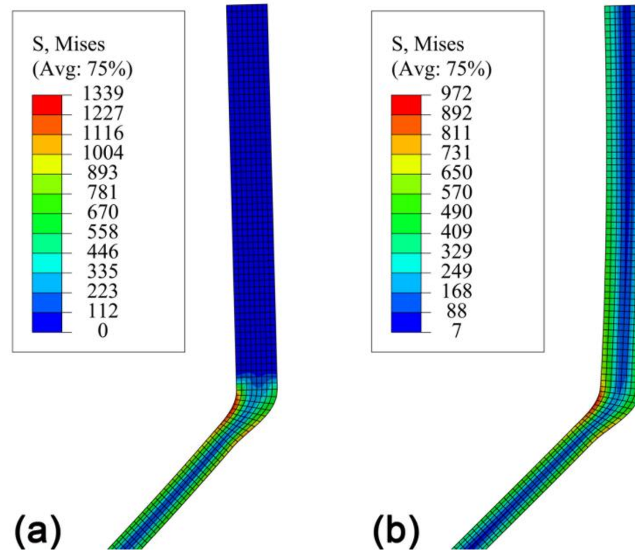

Figure 24: Stress distribution across the symmetric section of the probe in (a) a fixed mount, and (b) a floating mount assemblies at 125 μm overdrive.

For the floating mount assembly, it was observed that there were 3 regions where the deformed probe contacted the inner surface of the guide cylinders (A, B, and C in Figure 25). All of the contacts were areal; although the contact at A is much more confined than the others (B and C). Normal forces were extracted at all nodes on the contact area, and the total friction force opposing the sliding motion was calculated by multiplying the friction coefficient of 0.12 to the sum of all normal forces. It was found that the total normal force from the points of contacts was 2.141 gf, and the corresponding friction force opposing the motion was 0.257 gf, which accounts for only 3.55% reduction in the contact force for the floating mount assembly. Therefore, it was concluded that the contact area and the friction force have minimal effect on the contact force measured at the bottom of the probe.

The resultant MS and CF were summarized in Table 2 which clearly indicated that the floating mount probe assembly was much more desirable in reducing both MS and CF than fixed mount, with 27% and 15% reduction in MS and CF, respectively. Based on these results, fixed mount technique was excluded, and only floating mount assembly was taken into consideration for the probe needle design optimization in the next chapters.

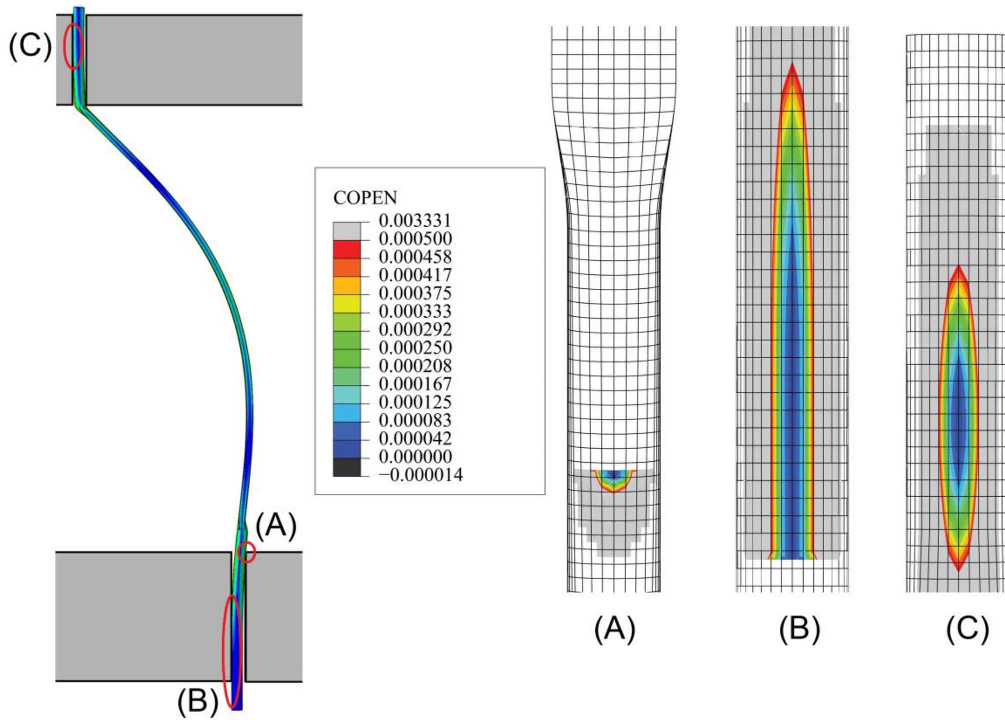

Figure 25: Regions of contact for floating mount assembly at maximum overdrive.

Table 2: Performance comparison between floating and fixed mount probe assemblies.

Mounting type	MS (MPa)	CF (gf)
Floating	972	7.248
Fixed	1339	8.509

5.5 Contact force (CF) simulation

It is known that in order to penetrate oxide layer formed on the surface and to make proper contact with the needle tip, the wafer ball bump should be indented by the tip by at least 0.5 μm [19,20]. On the other hand, the gradient of the vertical contact force during overdrive is generally designed in the range of 1.0 to 2.5 gf/mil (mil = 0.001 inch) for tungsten or tungsten-rhenium probes and 0.5 to 1.6 gf/mil for beryllium-copper or Paliney® probes [21]. The range of [1.0, 2.5 gf/mil] also has been employed as criteria for the probe design [2]. Since the probe material in this study was H3C which is one of Paliney® alloys, the maximum force gradient is limited to 1.6 gf/mil, while the minimum of 1.0 gf/mil is required to ensure the proper contact between the probe and the wafer bump. For the

force gradient range of [1.0, 1.6 gf/mil], corresponding contact force range at 125 μm overdrive was [5, 8 gf].

The indentation depth at this load range was determined by simulating the contact mechanism between the bottom of the needle tip and the top surface of the wafer bump. The needle tip was assigned a diameter of 63.5 μm to be consistent with the standard design, and it was considered to be rigid since its elastic modulus was much higher than the wafer bump. A commercial bump sphere model was employed for the wafer bump, with diameter and height of 105 μm and 85 μm, respectively [2, 22]. The deformable wafer bump and the rigid cylindrical probe tip were modeled as axisymmetric. The wafer bump model was meshed with 3256 2D quadrilateral elements and 3373 nodes (Figure 26(a)). Indentation depth was measured at the bottom surface of the needle tip in the load range between 5 and 8 gf. The plot of simulated CF against indentation depth in Figure 26(b) showed that the force increased almost linearly with the increase of indentation, and the indentations at 5 gf and 8 gf CF range were 1.16 and 1.85 μm (1.36% and 2.18% of the height), respectively. Since this indentation depths seemed adequate [23], CF range of [5, 8 gf] at 125 μm overdrive was adopted as a design constraint to determine the suitability of the design in the following chapters.

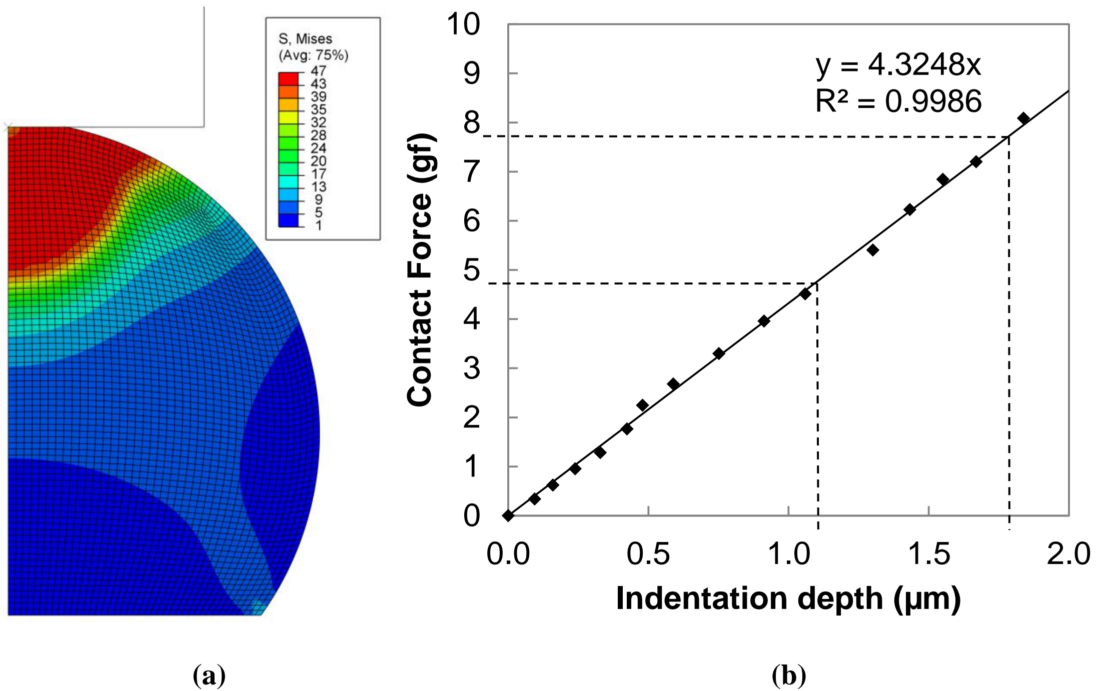

Figure 26: (a) Simulation of the wafer bump indentation and (b) the plot of contact force vs. indentation depth..

Chapter 6
Probe Geometry Optimization

Geometry optimization was performed to minimize the MS that occurs in the vertical probe at the maximum overdrive, while maintaining adequate CF. The optimization process primarily concentrated on modifying the geometry of the curvature of the cobra body, by employing the curvature function in Eq. (1) to a standard, flat-tip vertical cobra probe with geometry and dimensions in Table 1 and Figure 14. The overview of the optimization process was summarized in Figure 27.

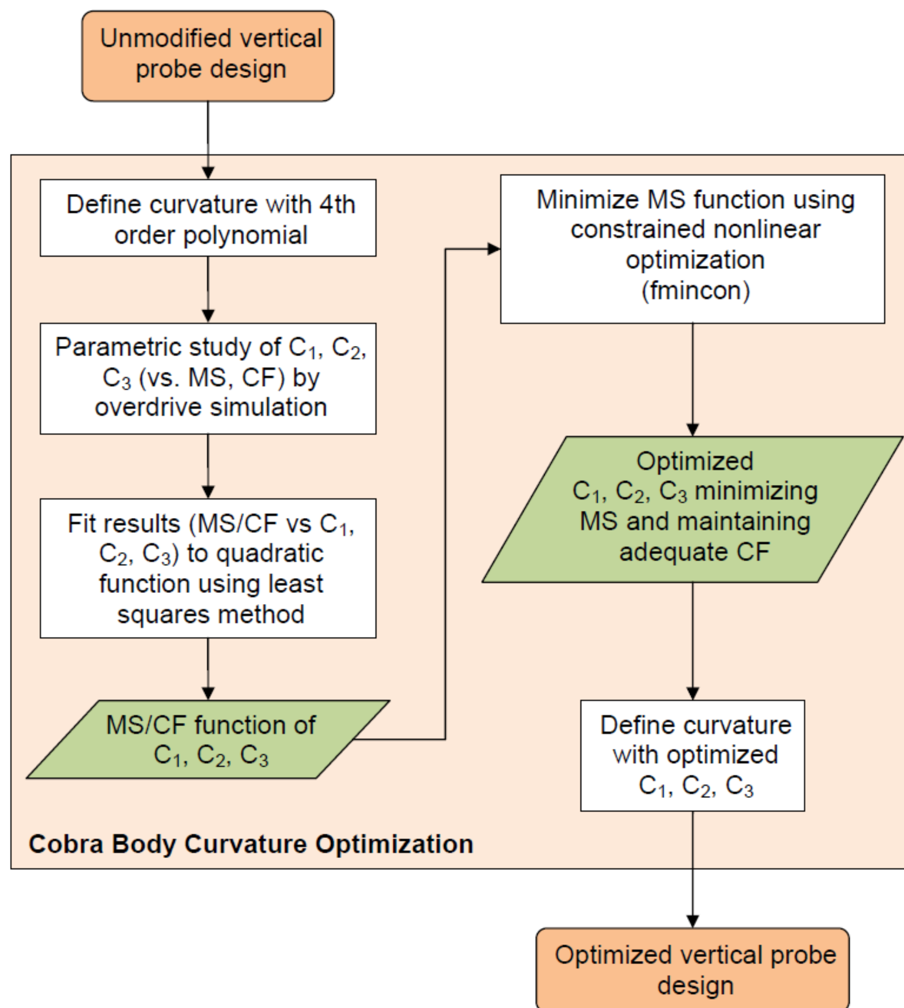

Figure 27: Overview of the optimization process.

6.1 The effect of overall probe dimensions

The effects of the major probe dimensions on the MS and CF were investigated with the standard design. Among the dimensions in Table 1, horizontal offset (O), cobra body pin length (B), and tip length (T) (Figure 14) were chosen to be the major dimensions. The effects on the MS and CF from independently changing O, B, and T were investigated by incrementally changing one dimension while keeping the other two constant, then performing overdrive simulations on the resultant designs. Parameter O, B, and T were varied incrementally by ±0.2 mm, ±0.75 mm, and ±0.4 mm, respectively, from their original dimensions in Table 1.

It is demonstrated in Figure 28 that higher values of all three dimensions, and subsequently larger overall probe geometry, resulted in lower MS. At the highest positive increments of O, B, and T (+0.2 mm, +0.75 mm and +0.4 mm from original dimensions, respectively), MS was decreased by 1.7%, 22.1%, and 16.6%, respectively, from those for standard design. Highest positive increments of O and T lowered the CF by 36.2% and 25.7%, respectively, but a slight increase of 4.5% was observed from the upper limit of B.

The above analyses demonstrated that the MS from the standard design can be reduced by increasing the overall size of the probe. However, this necessarily increases the probability of undesirable contacts between neighboring probes during overdrive and hampers the compactness, maintainability, and high probe density of probe card. Also the increase may cause the CF being below the design constraint as illustrated in Figure 28(a) and Figure 28(c). Therefore, it was concluded that changes of major dimensions is not an appropriate option to achieve the goal of design optimization, and a more rigorous optimization process needs to be adopted.

The effects on the MS and CF from combining different probe dimensions were also investigated by choosing O and T to be independent variables, and varying them in three different levels as indicated in Table 3. All possible combinations of the two parameters were modeled and simulated for overdrive.

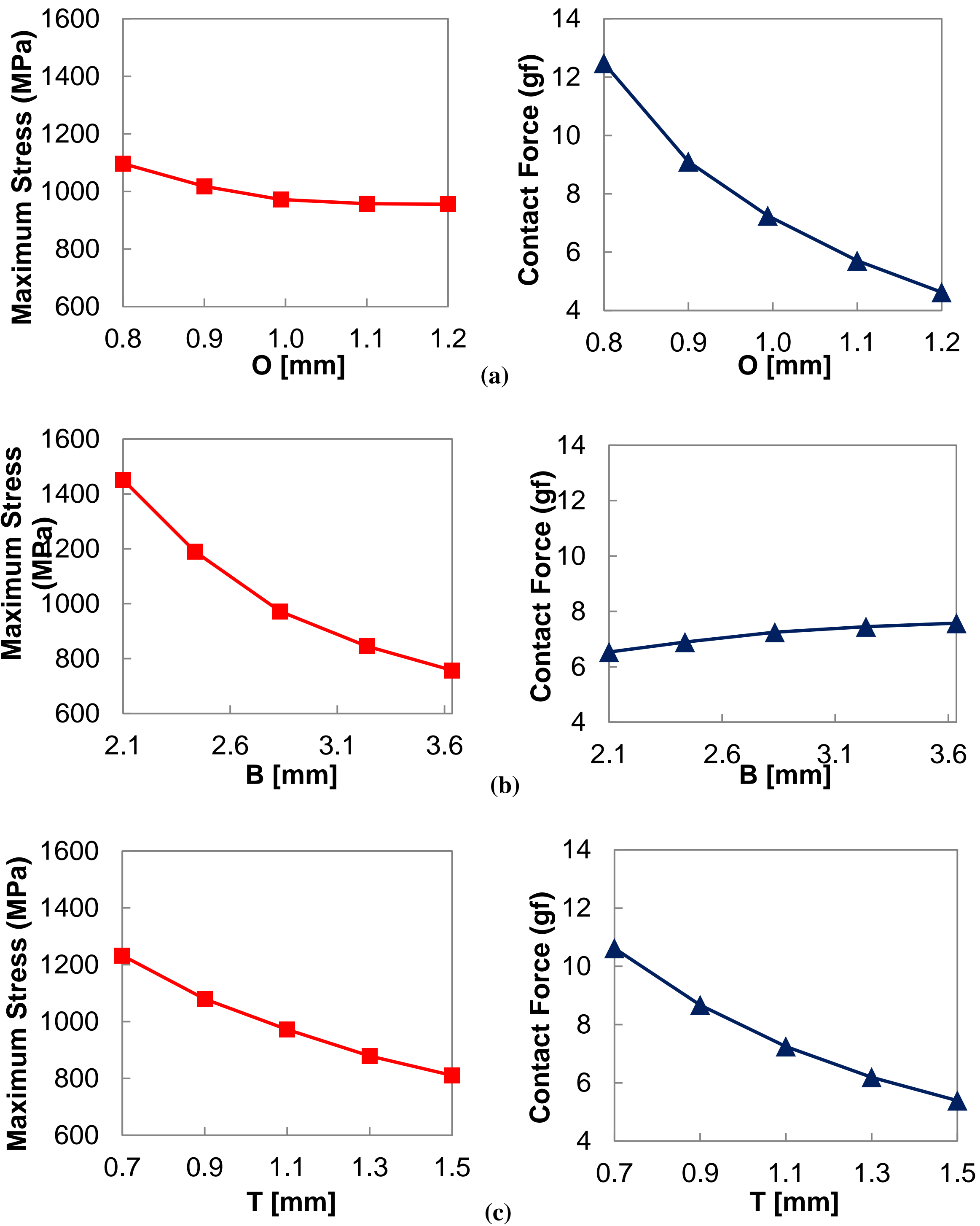

Figure 28: Variations of MS (Left) and CF (Right) within the ranges of: (a) horizontal offset, O, (b) cobra body pin length, B, and (c) tip length, T. The third data points in the middle of all plots are the results of the standard design.

Table 3: Level assignment to parameters O and T, and the design number for each combination of parameter levels.

(mm)	O1 (0.895)	O2 (0.994)	O3 (1.093)
T1 (0.920)	X11	X12	X13
T2 (1.227)	X21	X22	X23
T3 (1.534)	X31	X32	X33

MS and CF for each level simulated by FEA model were plotted in Figure 29. It is demonstrated that design X33 with the largest values of both O and T resulted in the lowest MS at 125 μm overdrive. Design X33 experienced the MS of 776 MPa and the CF of 5.29 gf, which accounts for approximately 20% and 27% decrease from the standard design for MS and CF, respectively.

In conclusion, it is demonstrated that the MS from the standard design can be reduced while keeping the CF above the design constraint of 5 gf, by reasonably increasing the overall size of the probe, as illustrated by design X33 in Figure 29. However, excessive increase of the parameters will result in the CF being below the design constraint as illustrated Figure 28(a), where the CF is below 5 gf when parameter O is increased by 0.2 mm from the standard design.

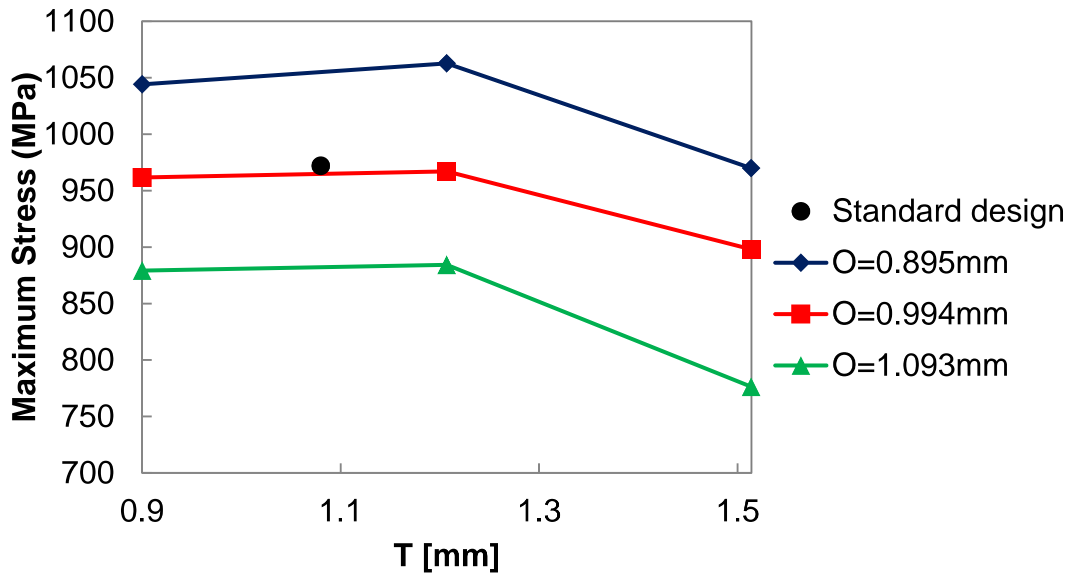

(a)

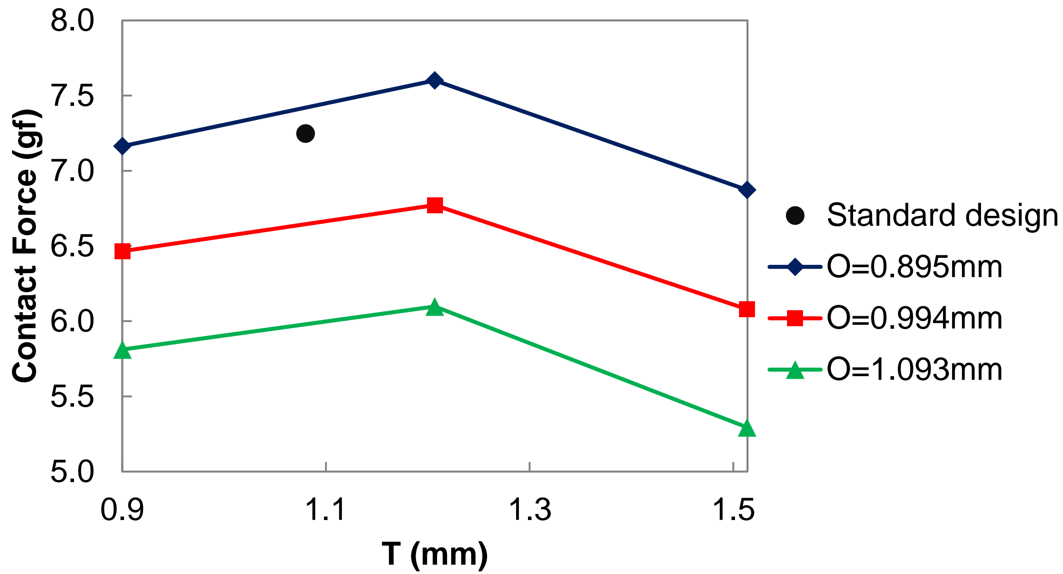

(b)

Figure 29: Performance of (a) MS and (b) CF at 125 μm overdrive, for all designs generated in Table 3.

6.2 Design constraints

Prior to optimization, design constraints were established for CF and the needle geometry. CF range of 5 gf to 8 gf, obtained from CF simulation, was chosen to be the inequality design constraint that must be satisfied by all design options. For the geometry constraint, since many vertical probe needles are spaced tightly together within a probe card, the variations of coefficients C_1, C_2, and C_3 in Eq. (1) were limited so as to restrict the amount of curvature deviation to ±5% from the standard design to avoid probe to probe contact during wafer probing. The insert part and tip length (I and T, respectively, in Figure 14 left) were left unchanged to avoid any complications in mounting into the guides.

6.3 Cobra body curvature optimization

The curvature optimization was performed to find the optimum curvature shape that would result in the lowest MS at maximum overdrive and the adequate CF satisfying CF constraint, while keep the design constraint. The first step of the optimization involves the formations of MS and CF functions with coefficients C_1, C_2, and C_3 as variables. For this, the optimized coefficient values of Eq. (1) proposed by Ref. [3] (-0.3505, 0.8546, and 1.3102, for C_1, C_2, and C_3, respectively) were applied to the standard design (Table 1) as a reference. Then effects of each coefficient on MS and CF were investigated by varying one coefficient incrementally while keeping the others, and overdrive was applied to the resultant design.

The plots in Figure 30 show the variations of MS and CF with respect to C_1, C_2 and C_3, respectively. Increases of C_1 and C_2 resulted in increasing trends in both MS and CF, while the increase of C_3 leaded the reduction of MS but increase of CF. The trends of MS and CF against C_3 were relatively linear; however, C_1 and C_2 caused quadratic variations in MS and CF, which suggested that for the curve fitting of MS and CF data within the tested ranges, the equation of the curve should be at least second degree polynomial. Since each coefficient affects different section of the cobra body curvature [3], it was assumed that no correlations existed between C_1, C_2, and C_3. Then, the MS and CF data sets in Figure 30 were fitted into the following quadratic functions:

$$MS = a_0 + a_1 C_1 + a_2 C_1^2 + a_3 C_2 + a_4 C_2^2 + a_5 C_3 + a_6 C_3^2 \quad (3)$$

$$CF = b_0 + b_1 C_1 + b_2 C_1^2 + b_3 C_2 + b_4 C_2^2 + b_5 C_3 + b_6 C_3^2 \quad (4)$$

The constants in Eq. (3) and (4) were estimated using least squares method and the results are presented in Table 4.

Table 4: Coefficients of MS (a_i) and CF (b_i) functions estimated by least squares method.

i	0	1	2	3	4	5	6
a_i	856.27	380.23	73.807	37.255	-7.4195	-45.092	5.9626
b_i	4.7461	9.2859	3.0948	2.2049	0.6659	1.0164	0.0430

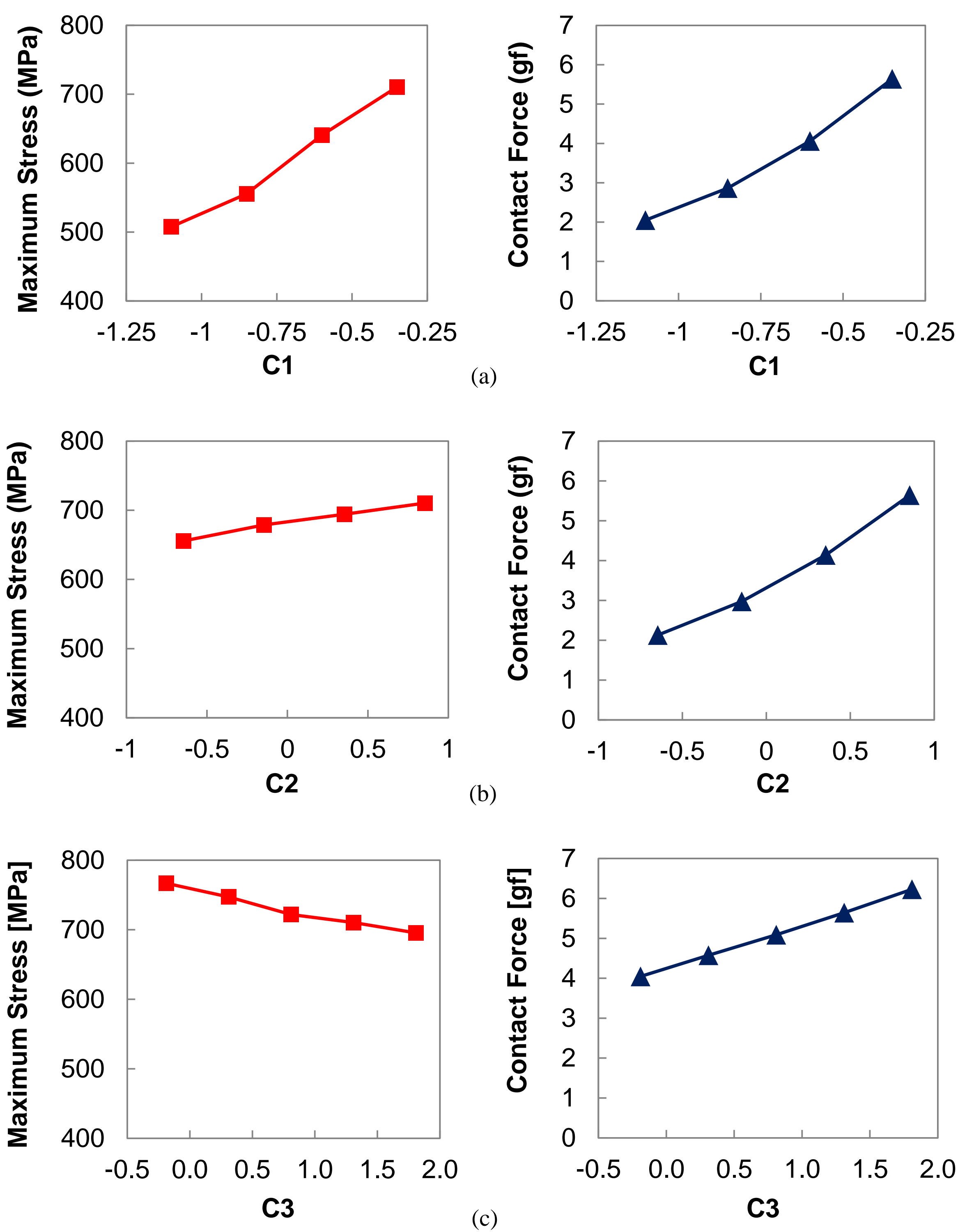

Figure 30: Variations of MS (left) and CF (right) at 125 μm overdrive, with respect to (a) C_1, (b) C_2, and (c) C_3.

The accuracies of MS and CF functions were tested by calculating MS and CF for various cobra curvatures with different values for C_1, C_2, and C_3, and the results were compared with those from FE simulations in Table 5. The average error of MS in Table 5 was only 0.45% with the standard deviation of 0.52%. CF error was even smaller with average value of 0.096% with the standard deviation of 0.064%. Therefore, proposed MS and CF functions were regarded as accurate enough to be utilized for the optimization.

Table 5: Comparison of MS and CF values predicted by Eqs. (3) and (4), respectively, and by FEA.

Test No	C1	C2	C3	MS (MPa)		Error	CF (gf)		Error
				Eq. (3)	FEA	(%)	Eq. (4)	FEA	(%)
1	-0.3505	0.8546	1.3102	709.64	710.42	-0.110	5.648	5.642	0.108
2	-0.6005	0.8546	1.3102	632.13	640.66	-1.349	4.062	4.060	0.061
3	-0.8505	0.8546	1.3102	563.84	555.32	1.513	2.863	2.865	-0.077
4	-1.1005	0.8546	1.3102	504.79	507.63	-0.563	2.051	2.050	0.046
5	-0.3505	0.3546	1.3102	695.50	694.26	0.178	4.143	4.140	0.073
6	-0.3505	-0.1454	1.3102	677.64	678.88	-0.182	2.971	2.973	-0.096
7	-0.3505	-0.6454	1.3102	656.08	655.67	0.063	2.131	2.130	0.048
8	-0.3505	0.8546	1.8102	696.39	695.45	0.135	6.223	6.227	-0.069
9	-0.3505	0.8546	0.8102	725.86	721.88	0.549	5.094	5.090	0.071
10	-0.3505	0.8546	0.3102	745.07	747.17	-0.282	4.562	4.574	-0.269
11	-0.3505	0.8546	-0.1898	767.25	766.87	0.050	4.051	4.045	0.140
					Average	0.452		Average	0.096

The next optimization was performed by minimizing the MS function in Eq. (3), while restricting the curvature deviation to below the geometry constraint and assigning CF constraint to Eq. (4). This was achieved by applying a minimization function, fmincon, in MATLAB to Eq. (3), which finds the minimum of a nonlinear multivariable function within a set of user-defined constraint functions. The geometry constraint function was defined as Eq. (1) with constraints of allowable geometry deviation by ±5%, and the CF constraint function was defined as Eq. (3), with minimum CF of 5 gf. The optimized coefficients C_1, C_2, and C_3 from fmincon are presented in Table 6. Based on the curvature defined by the optimized coefficients, a new FEA model was created, and the MS and CF were newly estimated. MS and CF were also predicted by Eq. (3) and (4) employing the optimized C_1, C_2, and C_3. The comparison of the results from FEA and Eqs. (3) and (4) in Table 6 suggested that the MS and CF equations were able to predict the optimized MS and CF values with high accuracy, with

maximum errors of approximately 1.910% and 2.048%, respectively. The deviation of the geometry was less than 5% which was within the constraint range.

Table 6: Optimized coefficients by fmincon, and the predicted MS and CF values by Eqs. (3) and (4), respectively, and by FEA.

C1	C2	C3	MS (MPa)		Error	CF (gf)		Error
			Eq. (3)	FEA	(%)	Eq. (4)	FEA	(%)
-0.4844	0.8546	1.8102	653.73	666.22	1.910	5.326	5.217	2.048

The MS and CF performance of standard probe design and the final optimized design were summarized in Table 7. It is obvious that the final optimized design resulted in the lowest MS, while satisfying CF and geometry constraints. The optimized MS (666 MPa) is much lower than the value which could be achieved by major dimension changes (757 MPa in Figure 28(b)). Note that the optimized design is particularly meaningful from the point of fatigue failure since the MS is only 37% of ultimate strength (1820 MPa), and likely below the fatigue limit. The shapes of standard design and the final optimized design are compared in Figure 31: Illustration of (a) standard design and (b) final optimized design.. Although slight change has been made only to the curvature section, significant reduction of maximum stress could be achieved which can reduce the operational fracture and increase the fatigue life of the probe needle.

Table 7: Summary of MS and CF performance at maximum overdrive.

Design type	MS (MPa)	CF(gf)
Standard Design	972	7.248
Final optimized design	666	5.217

Figure 31: Illustration of (a) standard design and (b) final optimized design.

Chapter 7
Fatigue Analysis

Based on the maximum stresses assessed by finite element analysis, the fatigue lives of different probe designs and mounting methods were calculated by first estimating the completely reversed Stress versus Life (S-N) curve, then taking into account the mean stress effects by using Smith, Watson, and Topper (SWT) approach. The fatigue lives of standard probe design with fixed and floating mount, and the optimized design with floating mount were analyzed.

7.1 Stress versus life (S-N) curve

An S-N curve is a collection of data from controlled experiments where a material undergoes a fully reversed cyclic stress (i.e. mean stress is 0) until failure occurs. The stress amplitude, S_a, is plotted against the number of cycles to failure, N. An S-N curve consists of two inclined lines representing low-cycle fatigue (LCF) and high-cycle fatigue (HCF), and a horizontal line representing the bending fatigue limit, as illustrated in Figure 32.

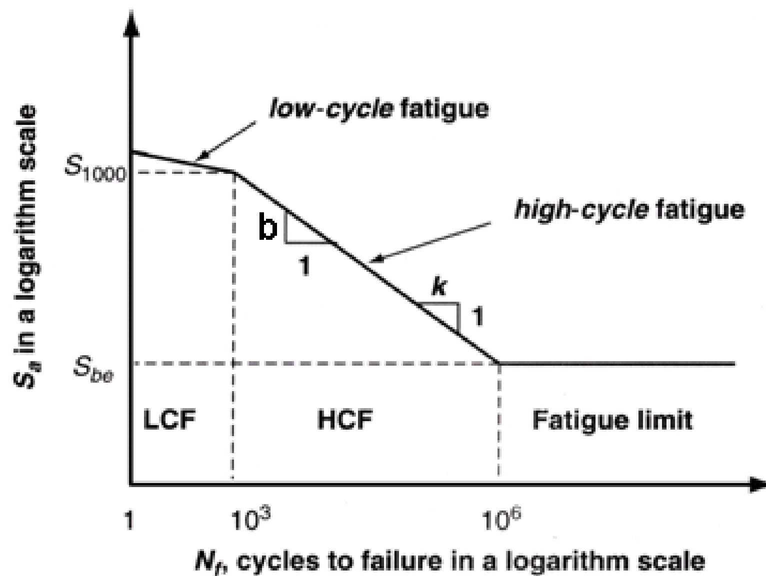

Figure 32: Schematic of an S-N curve for steels [27]

The S-N curve for steel is defined by the stress amplitude values at 1, 10^3, and 10^6 cycles, which are regarded as S_f', S_{1000}, and S_{be}, respectively.

7.2 S-N curve approximation

If the experimental data from fatigue test is not available, S_f', S_{1000}, and S_{be} can be approximated with respect to the ultimate tensile strength, S_{uts} [27]. It can be assumed that if the material fails at the first cycle (N=1), S_f' is equivalent to the S_{uts} of the material. For bending loads, S_{1000} can be approximated as 90% of S_{uts}. For estimating S_{be}, Eq. (6) is applied:

$$S_{be} = m_e m_t m_d m_s S_{uts} \quad (6)$$

where m_e, m_t, m_d, and m_s account for the bending fatigue limit, effects of type of loading, size, and surface finish, respectively. The values used for the reduction factors are summarized in Table 8. It is important to note that all estimation is based under the assumption that there is no notch on the specimen.

Table 8: Summary of factors which reduce the fatigue limit.

Reduction Factors	Values	Justification (Juvinall, 2006) [28]
m_e	0.5	Steels
m_t	1.0	Bending
m_d	1.0	d < 10 mm
m_s	0.5	Smooth, stamped specimen

7.3 Mean Stress Effect

It is important to emphasize that S-N curves are valid for completely reversed cyclic loads where the mean stress is zero. Since the loading during the overdrive process induces stress to the probe needle in a pulsating nature (i.e. from 0 to a positive maximum stress), cyclic stress oscillates about a non-zero mean stress, S_m. Therefore, to apply the S-N curve fatigue analysis to the overdrive process, S_a must be converted to the fully reversed nominal stress amplitude, S_{ar}, prior to calculating the fatigue life to compensate for the non-zero mean stress effect. There are variety of approaches for this conversion, such as methods developed by Goodman (1899), Gerber (1874), Morrow (1968), and Smith, Watson and Topper (SWT). It is known that SWT equation has the advantage of not relying on any material constants [x1], and therefore the SWT approach is employed for this analysis (Eq. (7)):

$$S_{ar} = \sqrt{(S_m + S_a)S_a} \tag{7}$$

7.4 Estimation of Fatigue Life

For estimating the fatigue life of different probe needle designs, methods developed by Juvinall [28] was employed. The Juvinall method provides the means of expressing the S-N curve with the following equation (Eq. (8)):

$$N_f = \left(\frac{S_{ar}}{10^a}\right)^{\frac{1}{b}} \tag{8}$$

where a and b are constants defined as Eq. (9) and (10), respectively:

$$a = \log \frac{(S_{1000})^2}{S_e} \tag{9}$$

$$b = \frac{1}{3} \log \frac{S_e}{S_{1000}} \tag{10}$$

To estimate the fatigue lives, S_{uts} was obtained from the tensile test performed on the H3C wire specimen, which was approximately 1820 MPa (Figure 17). It was approximated that $S_f' = S_{uts}$ and $S_{1000} = 0.9S_{uts}$, and S_{be} was calculated by Eq. (6) with the reduction factors listed in Table 7. S_{ar} was calculated from MS obtained from the finite element analysis using Eq. (7). Note that the $S_m = S_a$ for pulsating load, since the load is applied in a pulsating nature, with the minimum stress being zero. Finally, the fatigue lives were calculated by using Eqs. (8), (9), and (10). The estimation of fatigue lives for different probe designs are summarized in Table 9.

It is clear from the fatigue life estimation that reducing MS plays a critical role in increasing the fatigue life of the probe design. The advantages of using floating mount over the fixed mount are clearly evident, as the resultant stress reduction by 27% drastically increased the fatigue life by 463%. When the original design with floating mount is compared with the optimized design, a stress reduction of 31% increased the fatigue life by 668%. This fatigue analysis clearly emphasizes that stress reduction is important for prolonging the service lives of the probe needles.

Table 9: Fatigue life summary

Parameters	Original Design (Fixed)	Original Design (Floating)	Final Design
Maximum Stress (MPa)	1339	972	666
S_m (=S_a) (MPa)	670	486	333
S_{ar} (MPa)	947	687	471
Fatigue life (# of cycles)	19219	108129	830596

Chapter 8
Conclusions and Recommendations

8.1 Conclusion

The geometry of the floating mount type vertical probe needle was optimized by curvature optimization process to reduce the maximum stress during overdrive, while keeping the contact force and geometry within an adequate range.

Elastic modulus of the H3C probe needle were analyzed by conventional tensile test coupled with digital image cross-correlation technique to eliminate stress concentration at the grips. Force spectroscopy measurements were made on the 63%-Sn 37%-Pb wafer bump samples using atomic force microscopy to determine its elastic modulus. Material properties characterized by the experiments were inputted into the FEA models.

The cobra body curvature was modeled as a dimensionless 4th order polynomial and the effects of polynomial coefficients on the maximum stress and contact force were investigated. The simulation data were fitted into quadratic functions using least squares method for maximum stress and contact force. Optimal values of the coefficients were obtained by applying MATLAB's fmincon function to the maximum stress function with employing geometry and contact force functions as design constraints. It was illustrated that the maximum stress in the probe pin during overdrive process was effectively reduced from 1339 to 972 MPa by applying floating mount over the fixed mount, and further reduced to 666 MPa by applying the curvature optimization scheme. The final optimized design induced contact force of 5.217 gf, which was within the range of contact force constraint. The proposed design is expected to help prevent the probe breakage during overdrive operation and increase fatigue life.

Fatigue life estimation showed that the fatigue life increased from 19219 cycles to 108129 by applying floating mount over fixed mount, and further increased to 830596 for the optimized design.

8.2 Recommendation

There are several factors in this study that could be improved and pursued further. The following recommendations are provided below:

1) Various FEA simulations were simplified due to the heavy computation load and the large number of FE models that had to be simulated for the optimization process. The simulation for probe needle deformation and wafer bump indentation were performed separately, therefore the contact phenomenon such as scrub distances were not taken into account. The probe needle was modeled as a rigid component for the wafer bump indentation, which decreases the accuracy of the results. The results from this study can provide more realistic results if the probe needle and wafer bump simulations are combined.

2) In the geometry optimization process, the cobra body of the vertical probe needle was defined by the 4th order polynomial provided in Ref. [3]. The same optimization scheme can be applied to a probe with its cobra body defined by a different curvature model, with identical optimization constraints. Different curvature models should be tested since it is possible to obtain better probe performance by doing so.

3) The geometry constraint was designated a very conservative value of 5% deviation from the standard design. A more aggressive geometry constraint with higher deviation will allow further decrease in MS. It is suggested that a detailed interference/clearance study is performed on an assembly model with multiple probe pins placed closely together, so that the geometry constraint can be increased.

4) This study provides the means to optimize the geometry of standard probe needle design. However, the final optimized design was only validated via FEA, since there were no means to produce an actual prototype. The methods in manufacturing a probe pin with its cobra body defined by a custom curvature model should be pursued.

5) A mathematical approach was taken to estimate the fatigue life of the probe needle design. However, the calculated fatigue lives were not validated through experiments. It is recommended that similar approach indicated in Section 2.2.3 should be followed to perform the actual fatigue experimentations.

Bibliography

[1] Sasho S, Sakata T. Four Multi Probing Test for 16 bit DAC with Vertical Contact Probe Card, IEEE Test Conference 1996:86-91.

[2] Chang H-Y, Pan W-F, Lin, S-M, Investigation of Contact Behavior and Design of Vertical Probe for Wafer Level Probing, IEEE Trans Components, Packaging, Manufacturing Technology 2012;2(4):710-718.

[3] Chiu J-T, Chang D-Y. A new probe design combining finite element method and optimization used for vertical probe card in wafer probing, Precision Engineering 2009;33(4):395-401.

[4] Hauck T, Muller WH. Large deformation of beam columns - a closed form solution and design guide for vertical buckling probe needles, Proceedings of the IEEE 11th International Conference on Thermal, Mechanical & Multi-Physics Simulation, and Experiments in Microelectronics and Microsystems, 2010:1-3.

[5] Hauck T, Muller WH, Schmadlak I. Nonlinear buckling analysis of vertical wafer probe technology, Microsystem Technologies 2010;16(11):1909-1920.

[6] Iwai H, Nakayama A, Itoga N, Omata K. Cantilever Type Probe Card for At-Speed Memory Test on Wafer, Proceedings of the 23rd IEEE VLSI Test Symposium, 2005:85-89.

[7] Comeau AR, Nadeau N. Modeling the Bending of Probes Used in Semiconductor Industry, IEEE Trans Semiconductor Manufacturing 1991;4(2):122-127.

[8] Takahiro I, Sawada R, Higurashi E. Fabrication of micro IC probe for LSI testing, Sensors and Actuators 2000:80126–131.

[9] Lee K, Kim B.MEMS spring probe for non-destructive wafer level chip test, Journal of Micromechanics and Microengineering2005;5(5):953-7.

[10] Taber FL, An introduction to area array probing, Proceedings of the 8th IEEE SouthWest Test WorkShop, 1998:277–281.

[11] Beiley M, Leung J, Wong SS, A micro-machined array probe card-fabrication process, IEEE Trans Components, Packaging, Manufacturing Technology 1995;18(1):179–183.

[12] Zimmermann KF, Si probe-a new technology for wafer probing, Proceedings of the 5th IEEE SouthWest Test WorkShop, 1995:106–112.

[13] Pardee B, Fulton B, Using MLO packages to build vertical probe space transformers, Proceedings of the 12th IEEE SouthWest Test WorkShop, 2002:1–25.

[14] Byrnes HP, Wahl R. Contact for an Electrical Contactor Assembly. United States Patent 4027935; 1997.

[15] Maekawa S, Takemoto M, Kashiba Y, Deguchi Y, Miki K, Nagata T. Highly reliable probe for wafer testing. Proceedings of the 2000 Electronic Components and Technology Conference 2000:1152-1156.

[16] Chao YC, Lee YJ, Liu J, Shen GS, Tsai FJ, Liu DS, Shih MK. Development of probing mark analysis model [IC testing]. Proceedings of IEEE International Conference on Electronic Packaging Technology 2003:40–43.

[17] C Broz JJ, Rincon RM. Probe contact resistance variations during elevated temperature wafer test. Proceedings of IEEE International Test Conference 1999: 396–405.

[18] Wakuda M, Yamauchi Y, Kanzaki S, Yasuda T. Effect of surface texturing on friction reduction between ceramic and steel materials under lubricated sliding contact. *Wear* 2003; 254(3-4):356-363.

[19] Kataoka K, Kawamura S, Itoh T, Suga T, Ishikawa K, Honma H. Low contact-force and compliant MEMS probe card utilizing fritting contact. Proceedings of IEEE International Conference on Micro Electro Mechanical Systems 2002:364-367.

[20] Bates RD. The search for the universal probe card solution. Proceedings of IEEE International Test Conference 1997: 533-538.

[21] Otto Weeden, Probe Card Tutorial, 2003, [Online] Available at http://www.keithley.fr/com/data?asset=13263.

[22] Brizmer V, Kligerman Y, Etsion I. The effect of contact conditions and material properties on the elasticity terminus of a spherical contact, International Journal of Solids and Structures 2006; 43(18-19):5736–5749.

[23] Tunaboylu B, Testing of copper pillar bumps for wafer sort, IEEE Trans Components, Packaging, Manufacturing Technology 2012;2(6):985–993.

[24] Master, Raj N., et al. "Ceramic mini-ball grid array package for high speed device." *Electronic Components and Technology Conference, 1995. Proceedings., 45th*. IEEE, 1995.

[25] Integrated Technology Corporation, Introduction to Probe Cards – How They are Built & Tested, 1998, [Online] Available at http://www.swtest.org/swtw_library/1998proc/pdf/T2_itc1.pdf

[26] Huang, Jung-Tang, et al. "High density vertical probe card fabrication with low cost and high precision characteristics by using MEMS process." *Electronic Packaging Technology Conference, 2005. EPTC 2005. Proceedings of 7th*. Vol. 1. IEEE, 2005.

[27] H.J. Kwon, Fatigue and Fracture, Chapter 5: Estimated S-N Curve of a Component Based On Ultimate Tensile Strength.

[28] Juvinall, R. C., K. M. Marshek. 2006. Fundamentals of Machine Component Design, 4th ed., John Wiley, Hoboken, NJ.